Infrared Imaging of the Sub-millimetre Protocluster Near NGC 2068 in Orion B

by

Ashley J. Ruiter

A THESIS SUBMITTED IN PARTIAL FULFILMENT OF
THE REQUIREMENTS FOR THE DEGREE OF

MASTER OF SCIENCE

in

Astronomy

(Department of Astronomy and Physics)

Dr. George F. Mitchell

....

Dr. Joseph M. Hahn

....

Dr. David B. Guenther

....

Dr. Pierre Bastien

....

SAINT MARY'S UNIVERSITY

September 19, 2005

Canada

Contents

List of Figures

List of Tables

Acknowledgments

I will start by thanking my readers who have taken time out over Christmas holidays to read my thesis; my advisor George Mitchell, whom I thank for giving me the opportunity to observe with the CFHT, when I really didn't think it possible to have such an experience as a first year Master's student; David Guenther from whom I realized that main sequence stars were really cool too! And who always had advice when I would seek some; Joe Hahn, without whose course I wouldn't feel capable in pursuing areas of astronomy which I previously felt were not an option; and finally Pierre Bastien, whom I thank for setting a side the time at this time of year to help me out.

I would also like to thank Nick Tothill, from whom I learned many skills in the (mysterious) art of IR data reduction. Also all of the Saint Mary's astronomy graduate students (and noteworthy post doc) with whom I have spent some memorable times; Steve Craig, Jon Ramsey, Catherine Lovekin, Mina Rohanizadegan, Louise Edwards, Glenn Kacprzak (to whom I feel greatly indebted), and Amanda Karakas. AK and Robin Humble were most helpful in the early (but also frantic) stages of my thesis writing - thank you!

And of course I would like to thank my family, specifically my parents Ted and Victoria Ruiter, who have supported me in more ways than one since I can remember. Lastly I thank Chris Bernhard, who has been the greatest supporter and friend in my life for the past 5 years.

Infrared Imaging of the Sub-millimetre Protocluster Near NGC 2068 in Orion B

by Ashley J. Ruiter

Abstract: Sub-millimetre mapping of Orion B (L1630) using SCUBA on the James Clerk Maxwell Telescope has revealed a large population of compact cores (Mitchell et al. 2001). Using the CFHT-IR camera on the Canada-France-Hawaii Telescope, seven fields in NGC 2068 in Orion B were imaged in the near-infrared, both in a narrowband K continuum filter (2.260 μm) and in a narrow filter centred on the 2.122 μm line of H_2. The infrared images show many non-stellar and resolved features near several of the SCUBA cores, indicating the presence of embedded stellar objects and shock-excited gas.

We compare the infrared maps with the 850 μm sub-millimetre map, as well as a previously obtained map of CO $J = 3 - 2$ gas and H_2CO spectra in order to assess the likelihood of star formation for each SCUBA core.

September 19, 2005

Chapter 1

Introduction

The motivation for this infrared (IR) study is to develop a further understanding of the structure and evolution of the embedded star cluster near NGC 2068. Previous observations of the NGC 2068 protocluster at sub-mm wavelengths (Mitchell et al. 2001) have revealed structural information about the region, as sub-mm 850 μm observations from the Submillimetre Common-User Bolometer Array (SCUBA) trace the thermal dust emission of the young, potentially star-forming objects. Observations of dust are important, as many interstellar molecules will freeze out on dust grain surfaces, and so dust is an effective tracer of the distribution of mass in molecular clouds.

Young stellar objects (YSOs) in the NGC 2068 protocluster are shrouded in gas and dust, and hence are not visible in optical wavelengths. However we can obtain kinematic information from further sub-mm observations of high velocity CO gas, which can provide evidence of bipolar outflows emanating from young stars as their magnetic fields amplify their stellar winds, aiding in the launch of the outflow. CO mapping of NGC 2068 by Mitchell et al. found bipolar outflows centred on a few of the brighter 850 μm regions (cores). Such outflows are characteristic of the early stages of star formation.

Parsec-scale, filamentary structures are often observed in molecular clouds in

sub-mm (850 μm, tracing dust) wavelengths. These density-enhanced, often widely-separated regions are usually on the order of 1-a few pc in scale, and are clumpy. The clumpier regions within the filaments are more dense, about 0.1 pc in size, and number densities on the order of $n \sim 10^5$. They may be fairly asymmetrical in shape, or appear to be spherical. These dense structures detectable in sub-mm wavelengths are referred to as cores (or sub-mm cores; SCUBA cores). Formaldehyde (H_2CO) spectra can provide an estimate of kinetic gas temperature (Mangum & Wootten 1993), and this has been done for some of the SCUBA cores (Tothill and Mitchell 2001).

Infrared studies of regions in which star formation is thought to be ongoing will provide information about the physical structure of the region, as dust grains which are heated by any nearby hot stars will reprocess ultraviolet light and reradiate in the near infrared (K-band). Also, deeply embedded young and forming stars, their light reddened by dust, will be invisible at shorter wavelengths though signs of their presence such as shock-excited gas can be observed in the near-IR. Near-infrared observations obtained with the CFHT-IR camera on the Canada-France-Hawaii Telescope (CFHT) serve a dual purpose: to look for evidence of embedded stellar objects visible in narrowband K-band emission (2.260 μm), and to search for evidence for shocks in molecular hydrogen (H_2) line emission at 2.122 μm near these 850 μm cores.

The process of star formation is a short-lived one in terms of astronomical time scales; the more observations we can acquire of these astronomically interesting and

important yet heavily obscured regions, the deeper an understanding we can achieve about the evolutionary state of the young stars and the environment in which they form. Such types of observations will aid in the global understanding YSOs and their cluster environments, and the star formation process in general.

1.1 The Need For Observations

Cold, density-enhanced structures (sub-millimetre cores) associated with a larger filamentary region within a molecular cloud detectable in dust continuum emission, may or may not have an associated near-IR source. H_2 is the most prominent molecule in the interstellar medium, however it is not always readily detectable, as it must be heated to high temperatures by energetic phenomena (shocks) or nearby early-type stars (flourescense) in order for transitions to occur. The 2.122 μm vibrational line of H_2 is a well-known diagnostic for shocked and radiatively excited gas, and when observed in regions of active star formation the exciting mechanism is often shock-excitation by a stellar outflow. A core with associated filamentary or knot-like H_2 emission such as a Herbig-Haro (H-H) object or a more collimated or compact jet-like feature is evidence of shock-excitation by an outflow, and so the core in question is likely to contain a forming star. In context of star formation, the ro-vibrational 2.122 μm emission line of molecular hydrogen can be caused by either 1) a stellar outflow impacting upon and heating a nearby denser region of the interstellar medium , or 2) entrained dense clumps heated within the stellar outflow/jet itself. In both cases, the density of the region must be high enough, and must be heated

to temperatures on the order of 1000 K. H_2 has no permanent dipole moment since it is homonuclear, and so only electric quadrupole vibrational-rotational transitions are possible, unlike CO, where rotational transitions are permitted.

The shocked molecular hydrogen can reach temperatures greater than 10^3 K, though the molecule is readily collisionally de-excited due to the high density, and so the cooling times are short; on the order of a few years. The shocked hydrogen emission is a direct probe of the YSO jet, and so in some instances we are seeing YSO outflows in action so to speak. Thus, the hot H_2 is tracing the shock itself.

A core is considered to be pre-stellar if a star has not begun to form within it. However not all cores will form stars, even though the term pre-stellar suggests that a non star-forming core will in the future begin to form a star. Throughout this thesis, a pre-stellar object is defined as a sub-mm core that has not yet formed a star, and may or may not form a star in the future. Whether or not a pre-stellar core forms a star (or stars) is dependent upon its surroundings, such as turbulence and shocks, as well as other nearby forming stars which compete for mass accretion.

A core that is observed to have a nearby or coincident continuum K-band source is said to contain an embedded forming star, designated as Class 0 or later in the evolutionary scheme of stellar classification for early stellar evolution (Lada 1987; André et al. 1993). The K-band source need not be coincident with the core centre, as spatially the 850 μm emission of the core is 'fuzzy' and takes up a larger projected area than does the IR emission. The stellar classification which follows the pre-stellar phase (Class 0 to Class III) goes as follows: Class 0 – earliest phase, main accretion phase, collimated outflows; Class I – outflows less collimated, may be visible in

optical wavelengths pole-on; Class II – protoplanetary disc present (e.g. T Tauri), mass accretion ceases; Class III – may inhabit debris disc. If the core in question does not show any sign of an associated K-band source, nor has any evidence for shocks then it is likely to be pre-stellar, i.e. earlier than Class 0. The spectral energy distribution of a YSO will evolve as the star develops outflows and an accretion disc. The mechanism(s) responsible for launching YSO outflows is unknown, but magnetic fields and a disc wind are thought to play important roles. The four stages of stellar classification are described in more detail in § 1.2.

Observations of rotational CO lines are often used to trace molecular gas in the Milky Way and other galaxies, where stars may be forming. CO is a relatively abundant molecule in the interstellar medium ($n \sim 10^{-4} - 10^{-5}$ of H_2) and is usually optically thick. The CO molecule is readily observable since it has a lower critical density than many other interstellar molecules, allowing it to be detected (excited) at relatively low densities. The allowed rotational transitions contribute to its low excitation requirements, making it possible to observe low-temperature CO gas. H_2 on the other hand, has no allowed rotational transitions, and has much higher excitation requirements (i.e. higher temperatures are needed in order for any transitions to occur).

Observations of ^{13}CO and ^{12}CO reveal the presence of high-velocity gas in star forming regions, where the interstellar medium (ISM) environment is dynamically active. Assuming the isotopic abundance ratio for a particular region of a molecular cloud (i.e. $^{13}CO/^{12}CO = 1/60$) and assuming that the two CO species share the same excitation temperature T_{ex}, where T_{ex} is the temperature assuming a Boltzmann

population distribution for two transitional states, certain physical quantities can be deduced.[1] The radiation temperature of either species T_R can be determined from the assumed isotopic abundance ratio, see Mitchell 1991 (note that $T_R = T_{ex}$ in the optically thick limit). Then, the optical depth τ_ν as a function of line frequency (ν) of either species can be determined:

$$T_R = \left(1 - e^{-\tau_\nu}\right) \frac{h\nu/k}{e^{h\nu/kT_{ex}} - 1}. \tag{1.1}$$

Once the optical depth is found, N_l, the column density of CO molecules in the lower state can be calculated:

$$\tau_\nu = \frac{c^2}{8\pi\nu^2} \frac{g_u}{g_l} A_{ul} N_l \left[1 - e^{-h\nu/kT_{ex}}\right] \tag{1.2}$$

where g_u and g_l are the statistical weights of the upper and lower transition states, A_{ul} is the Einstein spontaneous emission coefficient [s^{-1}], h is Planck's constant, k is Boltzmann's constant, and c is the speed of light.

Further, in the local thermodynamic equilibrium approximation, $T_{ex} = T_{kin}$, where T_{kin} is the physical (kinetic) gas temperature. The optical depth τ_ν is related to the intensity of the medium I_ν via the equation of radiative transfer for a uniform medium:

$$I_\nu = \left(1 - e^{-\tau_\nu}\right) B_\nu(T_{ex}) \tag{1.3}$$

---

[1]For the optically thin case, T_{ex} can be found by taking a line ratio between two transitions, for example two rotational transitions of CO.

where B_ν is the Planck function, and is a function of T_{ex} (which is the same as T_R for $\tau_\nu \gg 1$, which is more often the case for ^{12}CO). However, due to the nature of the observational techniques used to collect sub-mm/radio data, T_R is not the temperature which is observed, but rather the instrument records the antenna temperature, T_A^*. T_R is aquired from the observed T_A^* by correcting for the beam efficiency η and the filling factor f, the latter which is often assumed to be ≈ 1.

In addition, CO channel maps are useful in estimating the orientation of the gas flow, which can help determine if a bipolar outflow is present near a specific core. When measurements of high-velocity CO gas are obtained the information is stored in a data cube, where an image is in fact a slice of a 3-dimensional map along the $x - y$ plane with coordinates $(x, y, z) = $ (spatial, spatial, velocity field). When the images are viewed at different values of integrated velocity (or channels) then it is clear where the higher and lower velocity gas are most dominant with respect to each core.

1.2 Classification of Young Stellar Objects

A star is said to have reached its pre-main sequence phase when it has accumulated $\gtrsim 90\%$ of its final main sequence mass, and begins to contract on the Kelvin-Helmholtz timescale (André et al. 1997). Young stellar pre-main sequence objects are classified into various groups in the literature: pre-stellar (often pre-protostellar), protostellar, Class 0, I, II and III. Lada (1987) postulated three 'classes' of young stars which are categorized mainly by their spectral energy distributions (SEDs)

and range from deeply embedded and young (Class I) to pre-main sequence (PMS) Class II & III objects. It later became clear that additional phases earlier than the Class I definition needed to be added to the scheme. Using Lada's original criteria in addition to more recent literature, the different stages of early stellar evolution for low mass stars are summarized in this section.

pre-stellar phase: Flat inner density profile with an increasingly sharp edge. A pre-stellar core may begin to collapse and form a star, or it may be destroyed by a passing shock and re-expand into the interstellar medium. Typical volumes of pre-stellar cores are on the order of 0.3 pc^3 (Goodwin et al. 2004), with number densities of $\sim 10^5$ cm^{-3}.

Protostellar phase: This refers to any stage between the pre-stellar phase and the ZAMS; class 0, I, II & III objects.[2] The protostellar phase is attained once the YSO has reached the Class 0 phase of evolution, i.e. once the embedded core has gone though its second collapse phase, to be explained in § 1.4.

Class 0:[3] This is the main accretion phase, with $T_{bol} < 70K$ (André et al. 1997), where T_{bol} is the bolometric temperature. The young YSO (age $\gtrsim 10^4$ years) will gather its mass from the surrounding envelope (typically ~ 1000 AU in radius) which made up the original core material, and is brightest in the sub-mm and IR wavelengths. The star and accretion disc (created from high angular momentum material falling toward the core from the circumstellar envelope) are deeply embed-

---

[2]Recently, it is a common thing to refer to Class 0 and Class I objects as 'protostellar', and Class II and Class III objects as 'pre-main sequence' stars.

[3]This class was first hypothesized by André 1993.

ded, and the mass of the envelope is significantly larger than that of the star-disc system (Mac Low & Klessen, 2004). Most of the luminosity is attributed to the accretion process, and accretion is thought to proceed at the rate

$$\dot{M}_{\rm acc} \sim \frac{c_c^3}{G} \tag{1.4}$$

where c_c is the sound speed (Shu 1977). A CO outflow may be visible, and will be very powerful and collimated compared to later stages of evolution.

Class I: At this stage the YSO is less embedded and can be seen in IR and optical wavelengths; the latter only when viewed along the pole direction. The outflows, though less collimated, contribute greatly to the clearing of the protostellar envelope material, and so the mass of the envelope is now much less than that of the star-disc system, lowering $\dot{M}_{\rm acc}$ by a factor of 10 (André et al. 1997). The spectral energy distributions are still broader than a corresponding blackbody curve ($70 < T_{\rm bol} < 650$ K), and rise longward of 2 microns (see figure 1.1).

Class II: This is the stage in which the star stops accreting mass, though it is still surrounded by a protoplanetary disc which causes the star to have an observable IR-excess. T-Tauri stars (both Weak and Classical T-Tauri stars) are a prototype of a Class II star, with ages on the order of 10^6 years. Their SEDs are similar to those of Class I, but are more flat longward of 2 microns. Average bolometric temperatures range between 650 and 2880 K.

Class III: These pre-main sequence stars no longer have a protoplanetary disc but may have a debris disc, and have temperatures higher than ~ 2880 K. Their

SEDs look somewhat like reddened black bodies, and there may be some mid-IR excess attributed to dust grains.

1.3 Molecular Clouds

Ninety-nine percent of the baryonic matter that lies between stars in galaxies is made up of gas. There are 10^{10} solar masses worth of gas in the Milky Way (Binney & Tremaine, 1994) of which the majority is hydrogen. Roughly half of this hydrogen is atomic, while the other half is in molecular form. Roughly 1% of the interstellar medium by mass is composed of dust; most of it carbon, which is thought to have formed in red giant stars and been expelled into the ISM by strong stellar winds.

Much of our visible Galaxy consists of stars ($10^{11}M_\odot$). They are either relatively isolated from each other (like our Sun), or in groups such as open star clusters, and the older, more populated halo-dwelling globular clusters. The ISM within the Galactic disc contains large-scale gravitationally bound clouds of dust and gas known as molecular clouds, which have average densities ranging from 10^2 particles/cm^3 (diffuse, e.g. ζ Oph) to 10^4 particles/cm^3 (dark clouds, e.g. Taurus). A molecular cloud will have regions of varying density owing to compressible turbulence, dissociation and ionization of material caused by nearby hot stars, and supernovae supersonic winds which may blow out or shock the medium, altering its structure. The denser regions of these clouds are where stars form. Molecules such as H_2 can form on dust grain surfaces in the dense, cold regions of the cloud; dust is an effective shield for molecules against the stellar radiation field. Stars do not form in
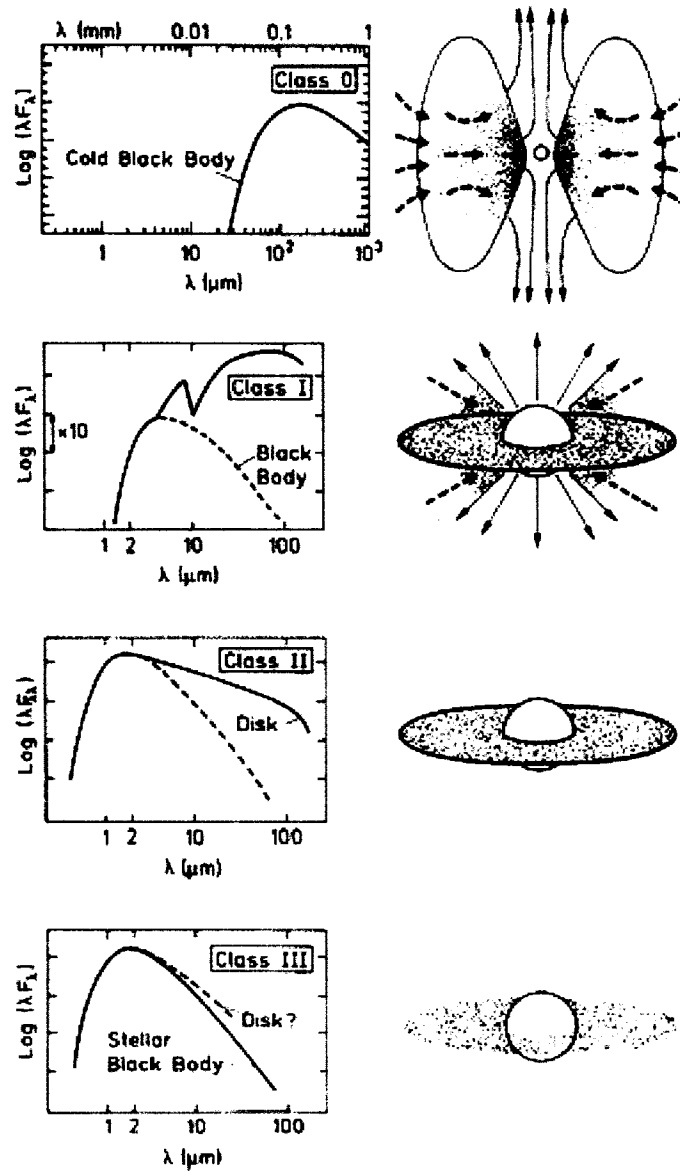
Figure 1.1: Spectral energy distribution of a young star in various stages of early evolution, and a schematic representation of the corresponding star-disc system. Figure is adapted from Bachiller, 1996. See text for further description.

the less-dense (0.01 particles/cm^3) inter-cloud region since the hydrogen is mostly

ionized there, i.e. from UV light coming from early-type stars which also raises the

temperature. On average the inter-cloud temperature is 10^3 K, but it can be as

high as 10^6 K in completely ionized regions. In the densest regions of molecular

clouds, temperatures are commonly as low as 10 or 20 K. Cold temperatures allow

for neutral atoms and molecules to coalesce and form clumpy structures throughout

the cloud.

How molecular clouds form is not well-understood. It has been hypothesized that

molecular clouds are transient objects that are formed by turbulent motions in the

ISM, and can be easily destroyed by these same turbulent processes (Klessen 2004).

The cloud can be broken down into two additional components. I will use the

term 'clump' to refer to a structure within the cloud but of much smaller scale and

having higher density than the ambient cloud, and the term 'core' referring to an

even smaller more compact object, usually found within a clump, out of which a

single star or multiple stars may form.

Giant Molecular Clouds (GMCs, such as Orion B) are ideal locations for star

formation since the gas and dust provide a shroud of protection against photoionizing

radiation emanating from nearby O and B-type stars, which may have formed within

the same cloud. The radiation flux from O stars peaks in the ultraviolet, and hence

these stars are efficient at destroying H_2 molecules, which make up a significant

portion of neutral interstellar matter important for core formation. In addition, the

stellar winds from young O and B stars aid in blowing away much of the molecular

material in their vicinity, dissociating the molecules and ionizing gas in an existing pre-stellar core or in a clump, also inhibiting star formation.

1.4 Star Formation

With sufficient density, cold cores made up of dust and gas within a cloud will undergo isothermal collapse. In some cases, shocks caused by powerful stellar winds, outflows or supernovae sometimes help in triggering the star formation process rather than inhibiting it, by increasing the density of the ISM (Elmegreen 1997). It is not always obvious from observations whether or not these dusty cores will form stars. A core that does collapse may form one or more stars. Recent simulations suggest that the fraction of YSOs in which one core will form multiple stars is well over 50% (Goodwin et al. 2004).

An embedded starless core will be visible in continuum dust emission and will have a temperature of $\sim$ 10 K. If the core is not destroyed by a passing shock, it will start to collapse isothermally, or nearly so, since in a dense core gas and dust become thermally coupled and the dust grains, which are very efficient at radiating away heat (Larson 2003, Mitchell 1991), control the core temperature. During the collapse the core will become very dense $((n)H_2 \approx 10^{10} cm^{-3}$, or 10^{-13} g/cm^3, Larson 2003), to the point where it is so optically thick that any heat generated by the collapse cannot readily escape. The increasing pressure is sufficient to slow down gravitational collapse and as densities continue to increase, the collapse halts temporarily. This is the end of the first collapse phase; the (nearly) hydrostatic core

continues to accumulate mass, and grows in temperature.

Once the core reaches a temperature of about 2000 K the molecular hydrogen starts to dissociate, absorbing energy. The core once again resumes collapse and heats up quickly once all of the H_2 is dissociated in the core (Mac Low & Klessen 2004) and ionization sets in. Gravity then cannot overwhelm pressure and the collapse is stopped. The stable core, or "protostar" with a mass of $\lesssim 10^{-2}$ $M_\odot$ will become a class 0 star.[4]

Matter does not flow directly onto the star from a surrounding envelope of material from which the core formed but rather rotation and magnetic fields aid in flattening the circumstellar envelope closest to the star's equator (Larson, 2003). An accretion disc will develop and the young star will be increasingly visible in the infrared. Once the star develops outflows and blows away much of the surrounding dust, it may also be detectable in the optical. Typical outflow velocities are $\gtrsim 100$ km/s. These powerful outflows are effective in dispersing and heating the medium around the star. This offers an opportunity to observe the most prominent molecule in the ISM, H_2. Normally, molecular hydrogen is cold, and cannot be observed directly. However when H_2 is heated by shock-excitation[5] up to temperatures of 1000 K, the 2.122 μm $v = 1 - 0, J = 3 - 1$ transition can be observed.

---

[4]This process is applicable to low-mass stars. In the case of high-mass star formation (see e.g. Stahler et al. 1997), hydrogen burning begins earlier on; during the accretion phase.

[5]Often times molecules are dissociated in shocks. Dissociation of H_2 will be inhibited If the magnetosonic speed is greater than the shock speed, given that the shock itself is not dissociative (shock velocity $\lesssim 50$ km/s). In this case ions will be deposited ahead of the shock, and collisions occurring ahead of the shock will remove energy from the shock, lowering the temperature.

Ignoring external pressure, an isolated spherical cloud of gas with uniform pressure P_c and temperature T_c will collapse to form one or more stars if the gravitational energy is sufficient:

$$\frac{3}{5}\frac{G M_{\rm c}^2}{R_{\rm c}} \gtrsim 4\pi R_{\rm c}^3 P_{\rm c} \qquad (1.5)$$

where M_c is the mass of the cloud, R_c the cloud radius, and G is the gravitational constant (Dyson and Williams, 1997). The cloud pressure is directly related to the kinetic properties of the cloud (i.e. temperature):

$$P_{\rm c} = \frac{3M_c kT_{\rm c}}{4\pi R_{\rm c}^3 m_{\rm H}\mu} \qquad (1.6)$$

where $m_{\rm H}$ is the particle mass (in this case hydrogen) and μ is the mean molecular weight, 1 for the neutral hydrogen atom. Equation (1.5) can be reduced to the following:

$$\frac{G M_{\rm c}}{5R_{\rm c}} \gtrsim \frac{kT_{\rm c}}{\mu m_{\rm H}} \qquad (1.7)$$

where the square root of the right-hand side of equation (1.7) is the sound speed of the cloud $c_{\rm c}$.[6] The time it takes for a sound wave to propagate across a cloud of radius R_c is $t_{\rm s} \approx R_{\rm c}/c_{\rm c}$. Using this relation, (1.7) can be rewritten as a function of cloud density $\rho_{\rm c}$

$$t_{\rm s} \gtrsim \left(\frac{15}{4\pi G\rho_{\rm c}}\right)^{1/2}. \qquad (1.8)$$

---

[6]The typical sound speed in a dark cloud is on the order of 0.2 km/s.

The free-fall collapse time is defined as the following:

$$\tau_{ff} = \left(\frac{3\,\pi}{32\,G\,\rho_c}\right)^{1/2} \tag{1.9}$$

and so equating (1.9) with (1.8), i.e. the condition for collapse, yields the following criterion:

$$t_s \gtrsim \frac{2\sqrt{10}}{\pi}t_{ff} \approx 2t_{ff}. \tag{1.10}$$

Equation (1.10) can also be written in terms of mass, a generally more useful interpretation. Using the expression for τ_{ff} and $R_c = \sqrt[3]{\frac{3M}{4\pi\rho_c}}$, the mass of the cloud M can be derived under these conditions:

$$M \gtrsim \left(\frac{3\,\pi^5}{32}\right)^{1/2} c_c^3\, G^{-3/2}\, \rho_c^{-1/2} \tag{1.11}$$

which also gives the condition for collapse. In (1.11), any mass greater than M will be unstable against gravitational collapse, and this critical mass limit is also called the Jeans Mass, M_J. A spherical pre-stellar clump whose mass exceeds M_J is unstable to gravitational perturbations and will undergo fragmentation.

1.4.1 Magnetic Fields

Magnetic fields are present throughout the ISM, with strengths ranging from about 3 to 30 μG (Mac Low and Klessen, 2004). Their strengths are observed predominantly through polarization effects (see e.g. Heiles et al. 1993, Weintraub et

al. 1997) and HI Zeeman measurements. Magnetic fields can provide support against gravitational collapse if the ionization fraction of the core or clump is high enough and if overall number densities are less than $n \sim 10^5$ cm^{-3}. For higher densities, the ionization fraction will decrease inhibiting the coupling of neutral particles to ions.

Cores (or clumps) which reach high enough densities will decouple from the magnetic field as the ionization fraction drops. Once the core is decoupled, i.e. the charged and neutral particles can be treated as two separate fluids, it is no longer stable to magnetic support and ambipolar diffusion may set in. In the classical theory of star formation, ambipolar diffusion was the accepted method by which star formation occurred on timescales on the order of 10^7 years (Larson 2003). By this process, when $n \gtrsim 10^5$ cm^{-3}, the ionization fraction can drop to $\sim$ a few x 10^{-6} (Klessen 2004) thereby allowing neutral particles to stream through the magnetic field lines even though charged particles (ions, electrons and some grains) will still be coupled to and hence supported by the magnetic field.

For a spherical clump of radius R, mass M, and uniform density ρ, gravity can only overwhelm magnetic support if the mass of the cloud is greater than a critical value, i.e. if

$$M > M_{\mathrm{cr}} \equiv \frac{5^{3/2}}{48\,\pi^2} \frac{B^3}{G^{3/2}\,\rho^2} \tag{1.12}$$

for a uniform magnetic field threading the cloud. The cloud is said to be subcritical if it is magnetostatically stable ($M < M_{\mathrm{cr}}$), and supercritical otherwise. The density profile of a collapsing clump obtained by ambipolar diffusion is $1/r^2$, with the outer

region being supported by the magnetic field, and the central region losing magnetic support, resulting in collapse.

Until recently it was thought that non-magnetic (hydrodynamical) turbulence would dissipate in molecular clouds much more rapidly than magneto-hydrodynamic compressible (MHDC) turbulence would, and the latter would provide magnetic support against collapse; however this idea is not supported by simulations (see Vázquez-Semadeni et al. 1997). Compressible turbulence decays on the order of dynamical timescales of a few to ~ 10 Myr (Larson 2003). It turns out that even strong magnetic fields cannot prevent the decay of turbulent motions, which are thought to play a very important role in molecular cloud support.

1.4.2 Turbulence

Where supersonic motions originate from in molecular clouds is not clear, but one possibility is that they are left over from the initial formation of the cloud (Mac Low 2002). Recent simulations of compressible turbulence find that turbulent support on global scales (the scale of a molecular cloud) aids in preventing star formation (Mac Low and Klessen, 2004), though turbulence on smaller scales can help to initiate core collapse. In order for a core or clump to become unstable to collapse in the presence of turbulent support, there must be dissipation of energy. A likely channel for the dissipation is in shock fronts as clumps collide with each other in a cloud.

Only recently have models of compressible turbulence been employed in the context of gravoturbulent fragmentation in molecular clouds, though a thorough quantitative discussion of the effects of turbulence in self-gravitating media is presented

in Sasao, 1973.

Since the dynamical collapse timescale of a molecular cloud is only $\sim$ a few Myr (Larson, 2003), clearly shorter than the typical stellar age, there must be a continuous supply of kinetic energy into the cloud which supports it against collapse. In order for a cloud to be turbulently supported, the turbulent decay time must be greater than the free-fall time, i.e. $\tau > 1$, where

$$\tau = \frac{\tau_d}{\tau_{ff}}, \tag{1.13}$$

and $\tau_d = E_{kin}/\dot{E}_{kin}$, where E_{kin} is the kinetic energy of the cloud, and $\dot{E}_{kin}$ is the rate of change of the kinetic energy due to turbulent decay. However, τ is typically found to be < 1 (Mac Low 2002) and so turbulence will decay on a shorter timescale than the free-fall time, which means that there must be some driving force which continuously injects energy into the cloud.

Some potential candidates for the driving mechanisms for turbulence are stellar jets and outflows, galactic rotation, and supernovae. Supernova-driven turbulence seems the most likely, since O and B stars are precursors of powerful supernova (SN) explosions, resulting in velocity dispersions of 10-15 km/s in the ambient medium. It's possible that molecular clouds are formed in such a scenario where gas is swept up in a SN-driven turbulent flow (Mac Low 2002). The main idea is that on large scales, molecular clouds are turbulently supported, but there is some mechansim(s) by which the turbulent support is lost on small scales, allowing star formation to

proceed.

Chapter 2

The Orion B Molecular Cloud

2.1 Previous Studies

The Orion B Giant Molecular Cloud, located at a distance of 390 - 450 pc, contains some of the nearest star-forming regions. It has been studied in J, H and K bands by Strom et al.(1976) and Li et al.(1997), in CS (Lada, Bally and Stark 1991; Lada 1992), and 2.2 microns (Lada et al. 1991). More recently it has been imaged in sub-mm wavelengths (Johnstone et al. 2001) as well as CO (Mitchell et al. 2001) and H_2CO (Tothill and Mitchell 2001). This thesis is the first H_2 study of the NGC 2068 region with the $v = 1-0$ $S(1)$ line, where $v = 1-0$ indicates the *vibrational* transition states $(1-0)$, the '(1)' represents the final state of the *rotational* (J) transition, and the S ($S-$branch) indicates that $\Delta J = 2$, so in this case, the rotational transition is $J = 3 - 1$ (Kwok 2005).

A CS map (see figure 2.1) shows part of the Orion B molecular cloud. The $J = 2 - 1$ transition of CS (98 GHz) is effective in imaging high-density structure $(n > 10^4$ cm$^{-3})$ comparable to densities of pre-stellar cores, and so is a good tracer of large-scale distribution of protoclusters in molecular clouds (Lada et al. 1991). Figure 2.2 shows a K-band (2.2 μm) map of the cloud for apparent K magnitudes < 12 (Lada et al. 1991). In the this figure, there are four regions which correspond

to regions of high surface density, with the NGC 2068 cluster being one of these regions. It is evident from figures 2.1 and 2.2 that if dense cores are good tracers of recent, current and future sites of star formation then stars do not form uniformly throughout molecular clouds, but rather are likely to form in discrete subgroups.

Figure 2.3 shows the 850 μm SCUBA map of Orion B North; note again the occurrence of discrete subgroups (clusters). Cores are clustered in regions near NGC 2071, NGC 2068, and H-H 24/25/26 (Johnstone et al. 2001). The process of determining the presence of a 'core' was carried out by an altered version of the algorithm *clfind* by the method described in Williams et al. (1994). There are 19 850 μm cores in total, 8 of which have a high surface brightness. The 850 μm dust continuum map shows regions which are high in thermal dust emission ($\sim$0.6 - 2.4 Jy). Since stars cannot form without the presence of dust, regions with a high concentration of dust are prime locations for star formation to occur.

In order to determine whether or not any of these cores are currently forming stars, the 850 μm continuum map will be compared with the K narrowband and H_2 line images, as well as the ^{12}CO $J = 3 - 2$ map and H_2CO spectra obtained by Mitchell et al. 2001 and Tothill and Mitchell 2001, respectively.
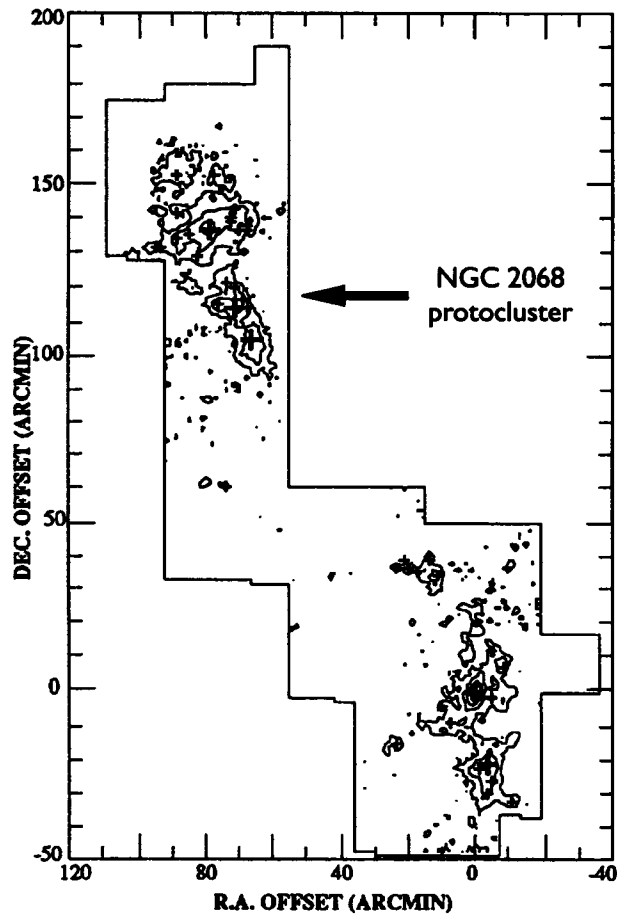
Figure 2.1: CS(2-1) map of part of the Orion B molecular cloud. The contours show integrated intensity over velocity range 7 − 13 km/s. The (0, 0) position corresponds to RA 05:39:12, Dec -01:55:42 (B1950). The northern part of the cloud consists of clusters associated with (top to bottom) NGC 2071, NGC 2068 and LBS 23, while Orion B South consists of clusters associated with NGC 2024 and NGC 2023. Figure adapted from Lada 1992.
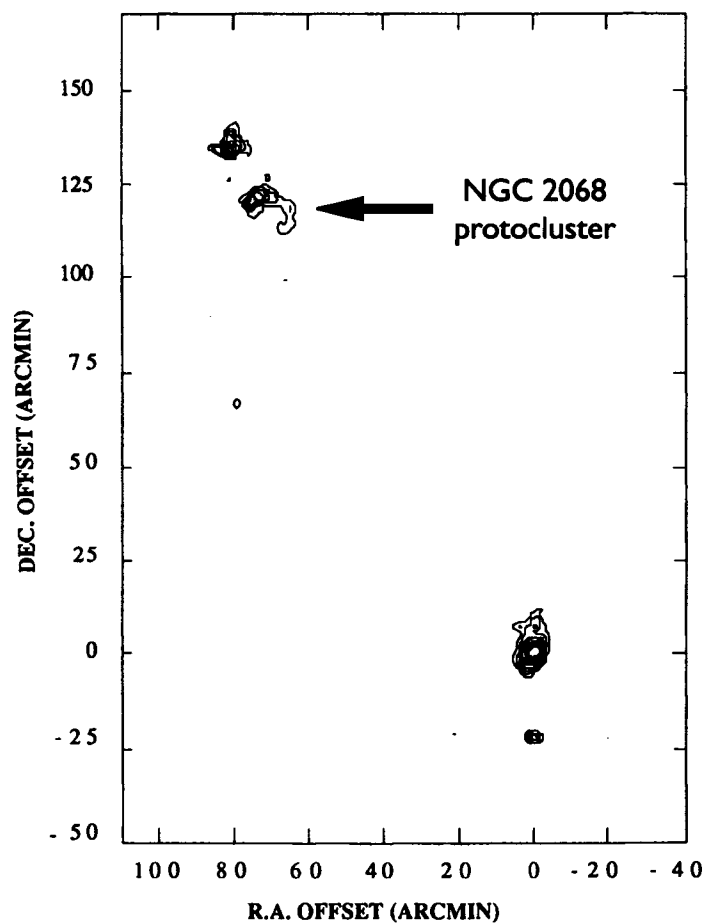
Figure 2.2: 2.2 μm surface density contours for Orion B. Coordinates are the same as in figure 2.1. The clusters were identified as regions where the source density was significantly above the background star density (1 square arcminute bins, with smoothing over adjacent bins). Lowest contour corresponds to 0.4 sources/arcmin². Figure adapted from Lada, DePoy, Evans and Gatley 1991.
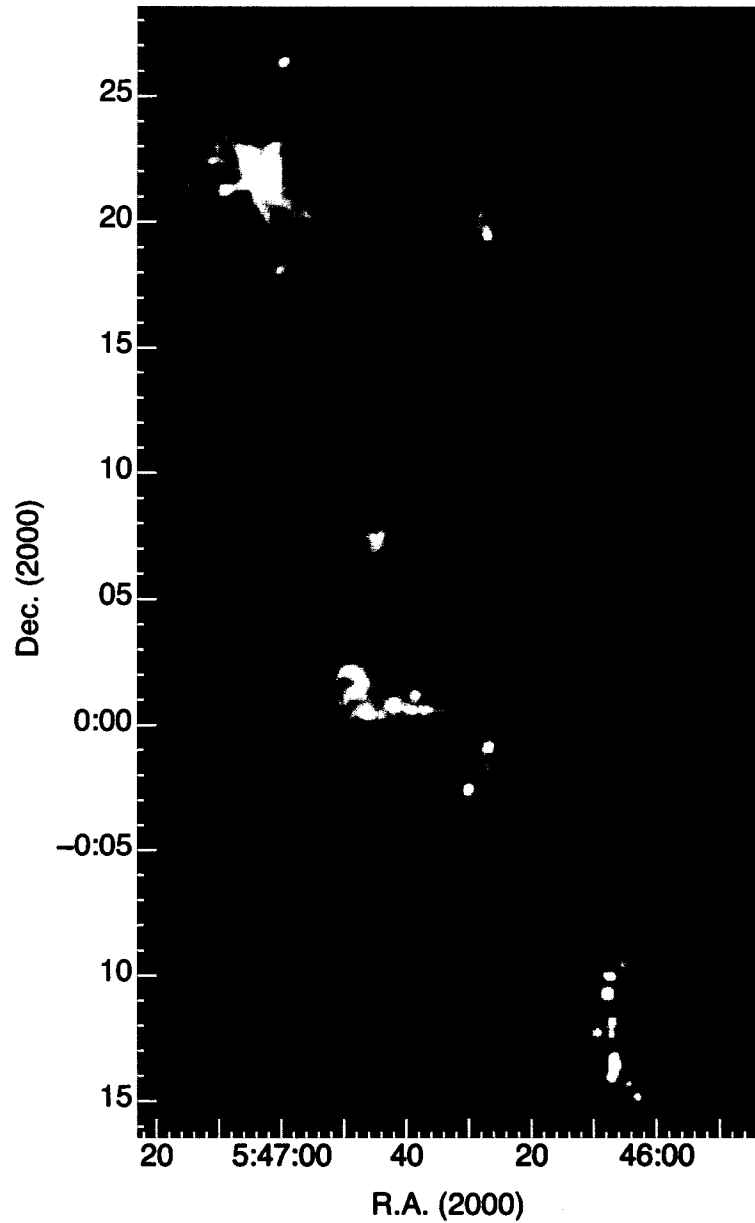
Figure 2.3: SCUBA 850 μm dust continuum map of the Orion B molecular cloud with J2000 epoch coordinates. The NGC 2068 protocluster is the filamentary structure located at a declination of 00:00:00. The figure is adapted from Johnstone et al. 2001.

Chapter 3

Observations

On February 27 2002, narrowband K continuum (2.260 μm, $\Delta\lambda = 0.6\mu$m) images were taken of six fields[1] in NGC 2068, as well as the United Kingdom Infrared Telescope (UKIRT) faint standard star 13, with the CFHT-IR camera on the CFHT on Mauna Kea. This faint standard star was chosen because of its close proximity to the region of interest. Each field was 3 arcminutes apart centre-to-centre, to allow for overlap, given the $(3.6)^2$ arcminute field of view of the CFHT-IR camera. The original intent was to image nine fields of NGC 2068. However weather conditions were poor (poor seeing) and so only 5 fields were observed in the continuum filter, and one field was imaged for only half of the desired time.

The CFHT-IR camera is an f/8 near-infrared detector. The HgCdTe detector is made up of one chip with the charge read out in 4 quadrants, has a total size of 1024 x 1024 pixels, with a plate scale of (0.211 ± 0.001) arcseconds/pixel.[2]

For these six fields, there were six 10 second exposures taken for each pointing of the telescope, for 5 pointings in each field. The pointings were 10" apart from central dither position to one of the corner dither positions (the "radius") as the pattern was arranged in a square configuration. A whole set of 5 pointings was to

---

[1]Please see the Appendix for a more extensive account of jargon pertaining to the data reduction process.

[2]More details about the CFHT-IR camera can be obtained at http://www.cfht.hawaii.edu/Instruments/Detectors/IR/CFHT-IR as of August 2005.

be performed twice for each individual field (i.e. two frames) for a total integration time of 10 minutes per field. In general, the telescope is dithered so as to eliminate the presence of bad pixels from showing up on the data once the image frames are combined. A nearby relatively blank patch of sky was chosen for sky frames to be used later for the purpose of sky-subtraction from the source images, and for these sky images the telescope was dithered in the same manner. Frames were taken in the sequence sky-souce1-source2-sky-sky-source2-source3-sky... etc. For calibration purposes, the faint standard star FS13 was imaged twice throughout the evening. The fields that did not obtain sufficient (or any) observation time were made up for in the following year.

On January 17, 18 and 19 2003, narrowband K continuum and H_2 line (2.122 μm, $\Delta\lambda = 0.2$ μm) images were obtained for seven fields in NGC 2068, as well as for FS 13. For the continuum data, three 20 second exposures were taken for five pointings in the fields where integration time was needed, for a total integration time of 10 minutes per field in continuum. For the line filter, two sets of three 60 second exposures for five pointings in each field were obtained, for a total integration time of 30 minutes on each field.

The integration times were chosen roughly to correspond to the difference in bandwidths of the two filters; the equivalent width of the K continuum filter is 4.1×(the H_2 filter). Conditions were clear with good seeing, but extremely windy, so integration time was not obtained for fields 7 and 8. Sky frames were obtained in a similar manner as they were for the previous year. Frames were taken in the

Table 3.1: Observation Coordinates of Orion B for 2003

Field	Right Ascension (J2000)	Declination (J2000)
	HH MM SS.S	dd mm ss.s
1	05 46 40.0	00 00 00.0
2	05 46 52.0	00 00 00.0
3	05 46 28.0	00 00 00.0
4	05 46 40.0	+00 03 00.0
5	05 46 52.0	+00 03 00.0
6	05 46 28.0	+00 03 00.0
7	05 46 40.0	-00 03 00.0
8	05 46 52.0	-00 03 00.0
9	05 46 28.0	-00 03 00.0

sequence sky-source1-sky-source1-sky-standard... etc. for each filter where possible. Flat field images were obtained for each filter using dome flats with 'lamp B' on and off. The flat field images obtained in 2003 were used for both data sets from 2002 and 2003, since they were of much better quality.

For the 5 point dither patten, the radius was set to 5 arcseconds. Five arcseconds between pointings is small enough such that the fields can be easily aligned later on by using common objects (stars) in each field. The standard star was imaged in H_2 three times on the first night, once the following night and twice the last night. It is best to image the standard star as often as possible as the detected flux of the standard, and hence of the source of interest, can change over time with weather conditions and airmass. On the first evening only H_2 data was obtained. The standard star was imaged twice in continuum throughout this observing run.

Chapter 4

Data Reduction and Analysis

4.1 Data Reduction

Data reduction was carried out using the Image Reduction Analysis Facility (IRAF) with SAOImage ds9, and STARLINK packages, primarily CCDPACK and KAPPA. This chapter covers the basic data reduction process. For a more detailed description of the processes, please see Appendix B.

The process of IR data reduction is quite different from the process of optical data reduction, since everything (sky, telescope dome, etc.) glows in the infrared making it difficult to detect the astronomical sources of interest.

CFHT-IR data is stored in data cubes; in other words one image file will have three dimensions. Two dimensions are spatial, just as in a regular image. The third dimension is the 'axis' along which the 2D images (integrations, or exposures) are stacked. Each individual pointing of the source images was sliced from the cube format into regular 2D images using the task *imslice* in IRAF [1]. The sliced source images were recombined to their corresponding pointing using the task *imsum* in IRAF, with *option* set to *average*. Using a combination of images with the exact

---

[1]There were usually three or six integrations per pointing; images composed of only a single integration such as some sky pointings, did not need to be sliced

same pointing position rather than simply one of its slices increases the signal to noise value.

Once the sky images were sliced, they were grouped according to their corresponding frame and their time of exposure (UT) relative to adjacent source images. Certain sky images were combined together and a resulting median[2] sky image was constructed. During data reduction, sky images that were taken closely spaced in time were combined (where possible), since in the K-band the sky is very bright - about 12.5 mag/arcseconds^2 (Jon Holtzman, private communication) and varies significantly over small time scales. The median sky frame, made up of approximately 13 individual sky exposures, was then subtracted from the corresponding source image(s). Sky subtraction was performed in IRAF with the task *imarith*. A similar process was carried out for the standard star images.

There were two final flat field images created for each filter; one with the 'lamp B off', and one with the 'lamp B on'. The final 'lamp off' image was subtracted from the 'lamp on' image to obtain an image of the intensity variations as a function of field angle, without the signal that would result from the dome slit, which was present (i.e. the dome was closed) during flat-fielding but not present whilst science frames were obtained with an open slit. This resulting flat field was used in the creation of the final normalized flat which was divided into each sky-subtracted image. The flat-fielded images of a given field were aligned using various tasks in CCDPACK and KAPPA. Once the images were aligned a mosaic was made for each

---

[2]The mean (average), midpoint (median) or mode pixel value of an image can be obtained by the task *imstat* in IRAF.

field. Eventually a map of the whole region was constructed; i.e. a mosaic of all 7 fields, one map per filter.

For the 2003 data, the images displayed what was referred to as a 'reset anomaly' whereby the images suffer a gradient in signal across each quadrant of the CCD owing to pixel-readout. This pattern was most evident in the first integration of each frame; the overall signal was lower. To help eliminate this feature, the first integration (slice) of the first pointing for each frame, source or sky, was not used in the creation of the final field images. In the case of the source images, this resulted in a loss of 1 out of every 15 images (2 out of 30 total), bearing little significance on the signal to noise value.

4.2 Coordinates

The equatorial coordinates (J2000) of the full mosaics were set by using the ESO digital catalogue as a preliminary estimate, and then adjusting the sky position using 2MASS (2 Micron All-Sky Survey) coordinates. The Digitized Sky at ESO is accessed through the Graphical Astronomy and Image Analysis tool (GAIA) under the Data-Servers menu. Through this image server, an optical image of NGC 2068 with RA and Dec coordinates could be downloaded. It was difficult to identify objects which were common to both the CFHT-IR mosaics and the ESO image, but a rough astronometric calibration could be made with the *Astrometry calibration* tool.[3] Once this was done, the *K* continuum mosaic was compared to the 2MASS

---

[3]Details on how to perform astrometry calibrations in GAIA can be found online on the Starlink website.

all-sky release Point Source Catalogue table of the same region (obtained through the IRSA Gator Query). Between 2 and 7 stars in each field of the mosaic were chosen to fine-tune the right ascension and declination. The H_2 mosaic was then calibrated to the continuum mosaic, using the *Fit to star positions* tool.

4.3   Photometry

The UKIRT faint standard star 13 was imaged in both filters for calibration purposes. The K-band (2.2 μm) magnitude of FS 13 is known, hence its flux can be determined. Vega is defined as having a magnitude of zero across all wavebands in the UBV system, and its flux density in the K band is 657 Jy (UKIRT). From this, one can calculate the flux density via

$$m_1 - m_2 = -2.5\log\frac{f_1}{f_2} \tag{4.1}$$

or

$$m_{\text{FS13}} = \frac{\log(f_{\text{FS13}}/f_{\text{Vega}})}{(-0.4)}. \tag{4.2}$$

Note that it is important to realize if the calibrated value for f is quoted as a flux (integrated flux) or a flux density (flux per unit wavelength, i.e. Janskys (Jy)). In this thesis I will adopt flux density units of Jy, and surface brightness units of Jy/arcseconds^2. Various units of flux density, magnitude and surface brightness are defined in C. J. Skinner (1996). Note as well that the narrowband K filter has a peak wavelength of 2.260 μm, where as the K broadband filter to which the

standard star is being calibrated is centred on 2.2 μm. However the broadband filter encompasses the waveband of the narrowband (NB) filter, so this should not affect results significantly.

Aperture photometry (with counts rather than magnitudes) was carried out using GAIA. A relationship between flux and airmass was sought for the standard star, thus one could simply derive the flux of an object based on the airmass at time of observation. However due to a limited data set and unfavourable observing conditions at times, there was no obvious relationship (i.e. linear) between flux and zenith distance (or instrumental magnitude and airmass). Instead, an average value of flux per count was defined for FS 13. A 'blanket calibration factor' was obtained for each filter, in each year, for a total of three calibration factors.

4.3.1 Measuring Counts in GAIA

Using the Image Analysis tool Aperture Photometry in data counts, one is free to set up various detector parameters, such as exposure time and instrument gain. The counts of a particular object of interest are measured interactively by drawing apertures around the objects. Apertures of different shapes (circular for stars or peak flux regions, or elliptical for extended sources) can be constructed and the aperture size can be easily varied. It is beneficial to try many different aperture sizes as well as sky aperture locations, or sky annulus sizes if an annulus is being used for the sky signal subtraction. An idea of the lower limit on what size aperture (in pixel radii) should be used to measure counts can be gaged by taking a slice

through the source in question, and examining the signal of the nearby pixels. All of the source signal should be encompassed in the aperture where possible.

For the point sources (i.e. the faint standard star), the sky signal was subtracted by taking the mean pixel value found in an annulus of blank sky surrounding the aperture. For extended sources a separate sky aperture was chosen for various locations of blank sky; blank is a relative term, as in many instances it was not discernable whether or not there was faint emission present over the source, and this resulted in a very large uncertainty in source flux density.

4.3.2 Continuum Subtraction

Large uncertainties in calculating pure H_2 flux densities are brought into play due to the fact that all of the H_2 data was obtained in 2003, and most of the K continuum data was obtained in 2002 (with the exception of all of field 6, and some of field 1). The gain on the instrument (electrons/ADU) is slightly different in each year, and also the reset anomaly was not an issue for 2002. Both of these present a problem in trying to properly calibrate data from different years which needs to be done in order to calculate the *pure* (continuum-subtracted) H_2 flux densities.

There is one field (6) for which data was obtained in 2003 for both filters, however field six contains only stellar sources - no extended emission - so one cannot obtain pure H_2 flux values of interesting objects. For field 1, half of the continuum data was obtained in 2002, with the other half in 2003. Field one by contrast to field 6 has a highly variable background with lots of interesting objects, and so both cases (2003 and 2002 continuum) were taken into account when determining the pure line

emission from field 1 objects. This also aids in putting an upper limit on the pure H_2

flux of all objects in the map, as field one is a perfect test case in how sky variability

and instrumental conditions impact the photometric results.

Chapter 5

K-band Results

In this chapter the K-band CFHT-IR images are presented. Many non-stellar emission features have been identified in the IR images toward several of the SCUBA cores. These features are named with labels corresponding to their celestial coordinates. The criteria for labeling features are 1) that the feature appears to be associated with H_2 emission, and/or 2) there is a sub-mm core nearby.

In instances where it is likely that a group of IR features are related to the same core, the emission features within the group are labeled under the same name, in the format HHMMSS.S±ddmmss.s. Usually the brightest IR feature in the ensemble of objects is chosen as the labeling coordinate. In instances where the flux of one of the objects associated with a labeled region is measured, the right ascension and declination of the object are tabulated in the format H:MM:SS.S±d:mm:ss.s.

In many instances, the IR emission is nearly coincident with a sub-mm core. The discussion regarding the association of the SCUBA cores with several of the IR emission features will be presented in detail in the next chapter. Note that the H_2 line images include *some* continuum emission, and all images presented are not continuum-subtracted, i.e. they are not *pure* line images. However pure H_2 line flux densities and surface brightnesses have been calculated, and the results are presented in this chapter.

Note that in the IR maps, specifically the H_2 map (fig. 5.2), there are horizontal lines that appear at declinations of $\sim$ +00:03:00, 00:00:00, and -00:03:00. This is mainly due to the 'reset anomaly' problem of the CFHT-IR chip. The lines are located at the location of the quadrant boundaries and are somewhat wide as a result of the mosaic-making process. As previously mentioned the CFHT-IR chip is composed of four quadrants, the charge being read out separately for each, and there is a noticeable gradient across each quadrant, specifically in the north-south direction, where North is at the top of each image, and East is to the left. Though it is possible to carefully smooth out the appearance of the images, the maps presented here have not been doctored; they are the fully reduced unaltered mosaics.
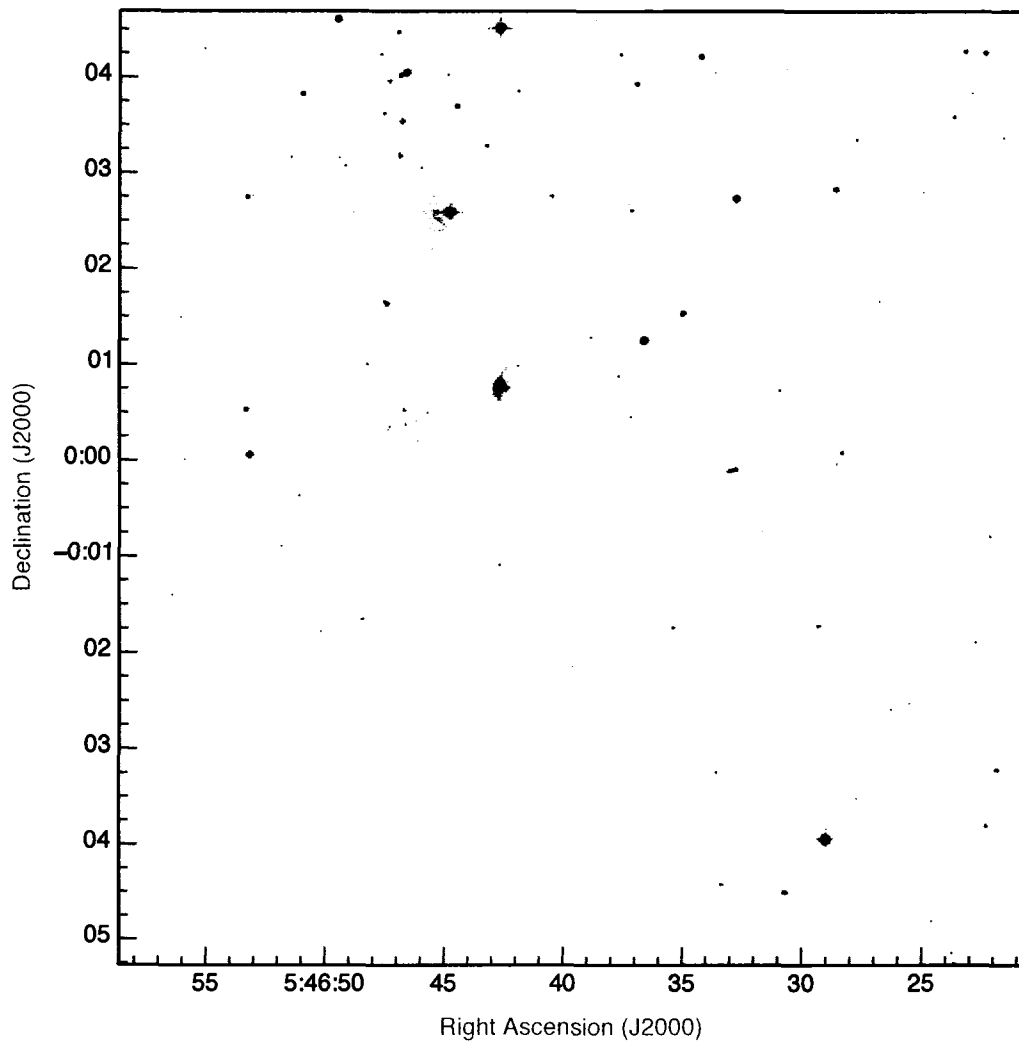
Figure 5.1: Narrowband K continuum map of NGC 2068 showing all seven fields.
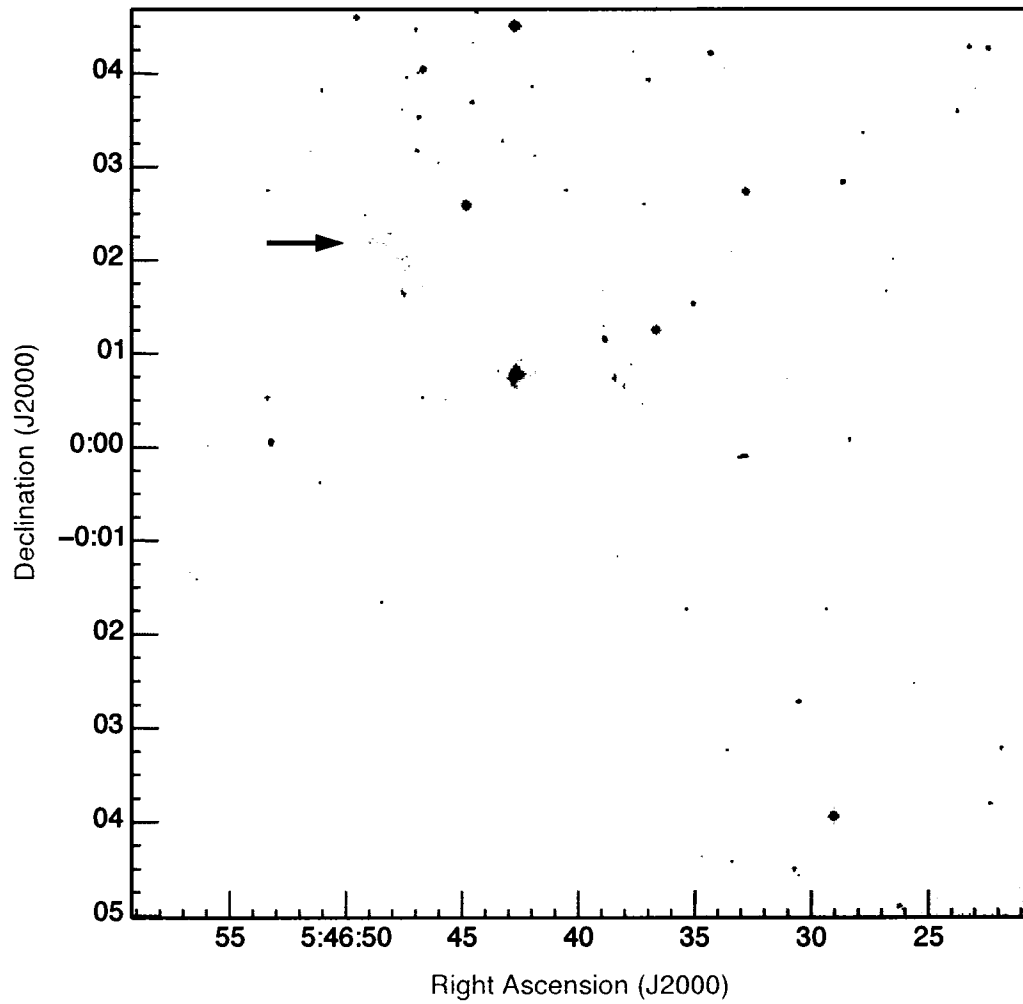
Figure 5.2: 2.122 μm map of NGC 2068 showing all seven fields. The arrow is showing the bright band of emission which is discussed in the text.
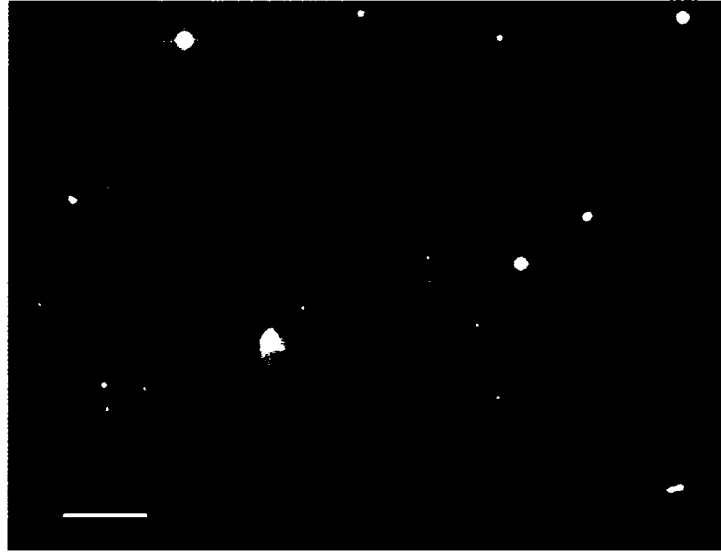
Figure 5.3: Central region of narrowband continuum map. This image is centred on coordinates RA 5:46:40.8, Dec +0:01:15.4.
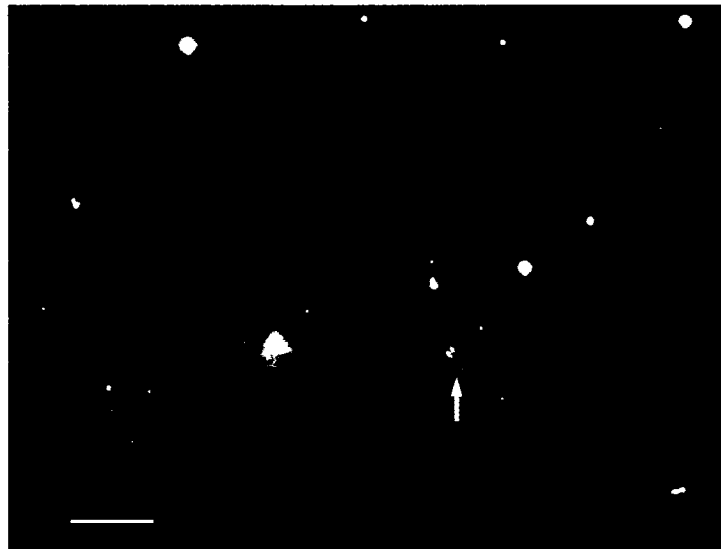
Figure 5.4: Central region of 2.122 μm map. This image is centred on coordinates RA 5:46:40.8, Dec +0:01:15.4. Note the extent of nebulous morphology (diffuse structure, knots, 'bowshock' indicated with an arrow) across the image, in contrast to the NB image.

Figure 5.5: north-eastern region of narrowband continuum map. This image is centred on coordinates RA 5:46:42.2, Dec +0:03:08.2.

One of the most striking features of the IR maps (see figure 5.2, the arrow) at first glance is the bright band of nebulosity ~ 2 arcminutes in extent in the vicinity of one of the brightest stars in the field. This star HD 38563 C, spectral type A0II (SIMBAD) looks as though it is responsible for most of the continuum flux seen surrounding it to the south-east, as this flux appears to be reflected starlight. The band of emission appears just above the bright, compact IR object associated with 054648.0+000141.6 (see figures 5.2, 5.4 and south-east corner of 5.5 & 5.6). The star HD 38563 N of spectral type B1.5V located north of the image boundary is thought to be responsible for the reflection nebula NGC 2068 (Grosso et al. 2004), and it is likely responsible for some of the nebulosity that is observed here. Ultraviolet photons from O and B stars can be absorbed by H_2 molecules (Lyman and Werner
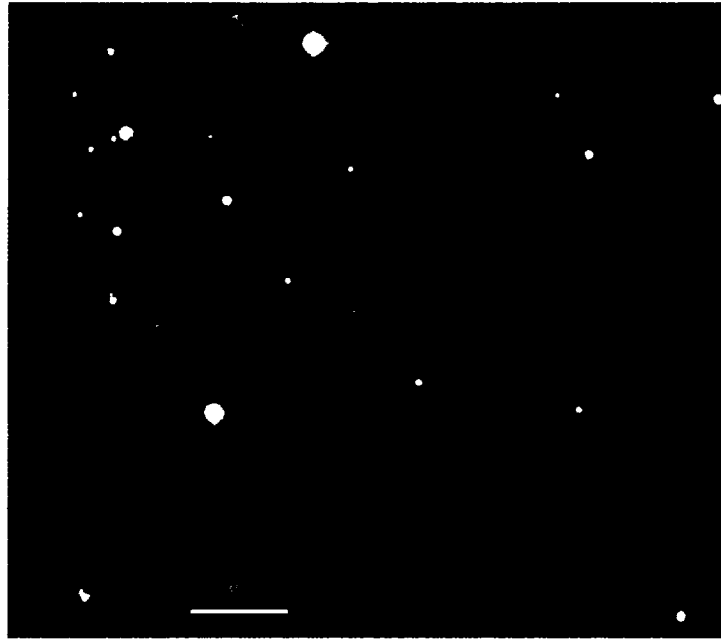
Figure 5.6: north-eastern region of the 2.122 μm map. This image is centred on coordinates RA 5:46:42.2, Dec +0:03:08.2

bands) causing them to be radiatively de-excited into ground-level excited states, resulting in fluorescence. If this region is a mixture of continuum and line emission, it's presumable that we are seeing reflected starlight of these bright stars by dust as well as fluorescence as just described. This slightly cone-shaped region can be likened somewhat to the star forming region Sharpless 106 (S106), a prominent H II region in Cygnus in which strong stellar winds from a late-type O star (S106 IR) have swept out bipolar cavities. S106 is one of the closest regions of massive star formation (Bally & Yu et al. 1998), though it is fairly obscured ($A_V \sim 20$). Dust lanes, possibly a stellar torus, aid in scattering some of the high-energy photons and are also made visible against bright background emission.

Field 2 (see table 3.1) contains some very faint H_2 emission (see figure 5.8).

Table 5.1: IR objects in NGC 2068 and their possible associated core(s). The objects are listed in order of increasing right ascension, and are mapped in figures 5.7 & 5.8.

Name	Assoc. Core	Brief Description
054626.3-000445.4	-	compact & patchy H_2; some continuum
054627.8-000052.8	47	very faint H_2 emission
054630.6-000426.6	-	H_2 knot; near star
054630.7-000235.4	51	compact H_2 jet; some continuum
054633.2+000001.8	42	binary? bright cont. & H_2, H_2 structures w/in 40"
054636.9+000056.7	38?	H_2 knot
054638.8+000050.5	34? 38?	H_2 "bow shock" feaature
054639.3+000114.7	34	bright, compact H_2 blob
054639.4+000142.6	34?	faint H_2 knots in nebulous region
054640.5+000052.8	34? 38?	H_2 knot
054640.9+000417.9	-	H_2 knot
054641.5+000306.5	-	several H_2 knots; "V"-configuration
054643.1+000052.2	35	very bright, extended H_2 & cont. emission
054645.1+000442.2	-	bright H_2 patch
054647.0+000027.0	39	cont. & H_2 knots/emission within 15"
054648.0+000141.6	32, star	compact, bright asymmetrical H_2 & cont. emisson;
	32, star	extensive "band" of H_2 & cont. emission
054649.0+000015.0	39	H_2 knot
054649.8+000054.6	39? 32?	very faint H_2 knot
054651.4+000026.0	39? 32?	faint H_2 knot
054651.5-000004.0	39?	several very faint H_2 knots
054654.7-000003.0	39? 43?	H_2 knot

These faint knots become noticeable only when the 'Blink images' command is used in GAIA, when the continuum and line images of the same region are aligned and compared.

There is a region consisting of diffuse gas and knots in a "V" configuration (054641.5+000306.5) visible in the line filter map but entirely undetected in continuum (see figure 5.9). Given the fact that these nebulous knots are observed in a region of star formation and have a Herbig-Haro-like appearance, they are likely
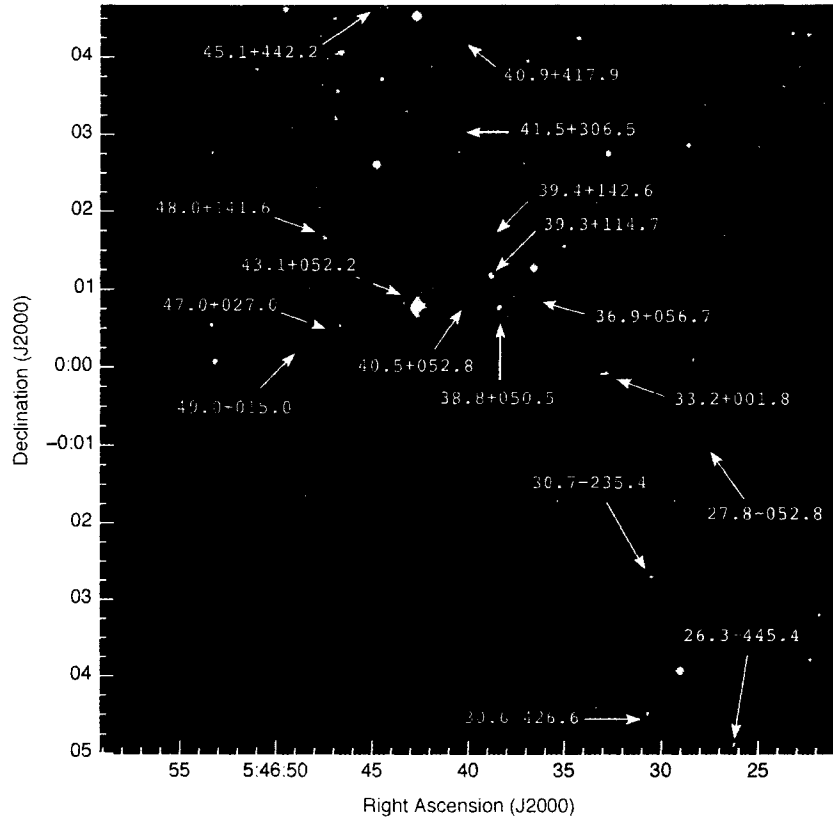
Figure 5.7: Map of NGC 2068 though the 2.122 μm filter. Seventeen of the 21 objects from Table 5.1 are labelled.

to be shock-excited H_2 but the excitation source unknown. One low surface brightness sub-mm core is located north of these H_2 features (Orisub-mm 30, Mitchell et al. 2001), but the offset of the H_2 knots from the core is > 1 arcminute, so a direct association is not obvious.

Farther to the north of these H_2 knots is a compact patch of emission detected strongly in the line filter and weakly in continuum (054645.1+000442.2, figure 5.10). Since the northern part of the field is closer to the star cluster NGC 2068 and the hot
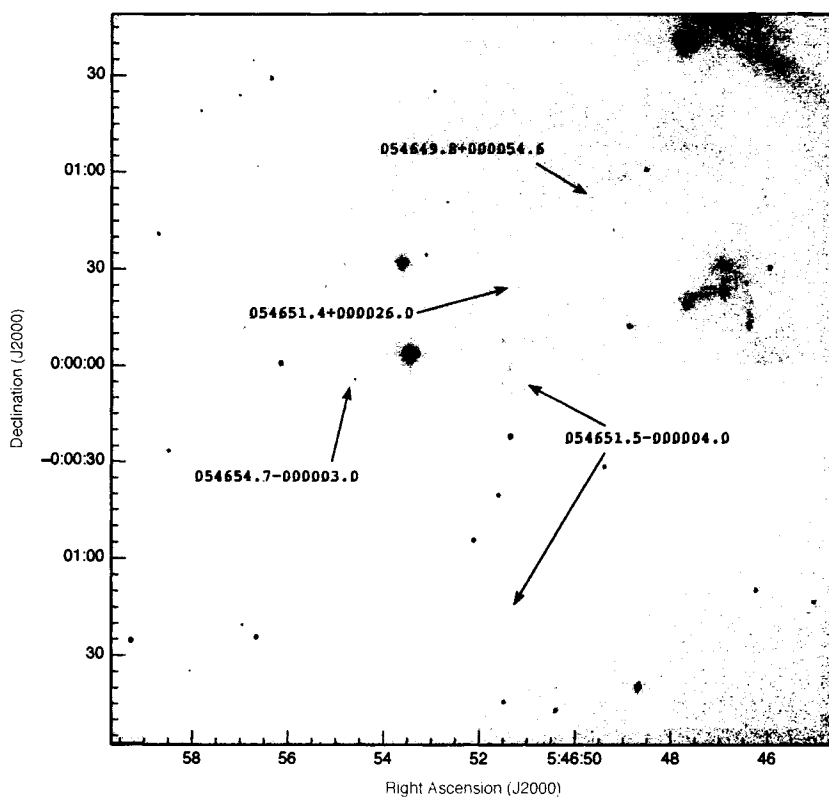
Figure 5.8: Four objects from Table 5.1. The south-east pointing arrowhead of 054651.5-000004.0 is located at the centre of four very faint knots each located ~ 10" from the arrow tip.

B1.5V star discussed earlier, it's possible that we're seeing UV fluorescence and some scattered starlight, but shock-excitation from an undetected YSO cannot be ruled out. A fainter H_2 feature (054640.9+000417.9) is visible in figure 5.10 south-west of 054645.1+000442.2.

In the southern-most field there are a few interesting H_2 features. The cigar-shaped object at 054626.3-000445.4 (figure 5.11) is also visible in the continuum image, is quite compact and bright in nature, and is possibly a stellar jet. However no 850 μm core is detected here in the SCUBA map (Mitchell et al. 2001). The H_2
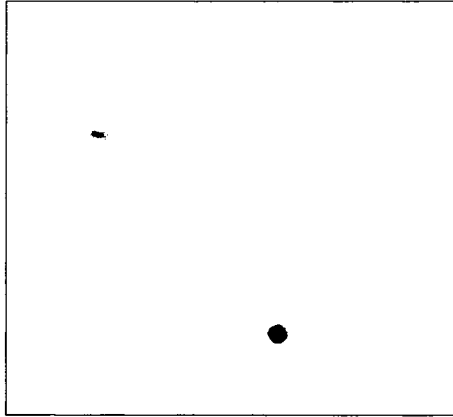
Figure 5.9: H$_2$ knots in 054641.5+000306.5.
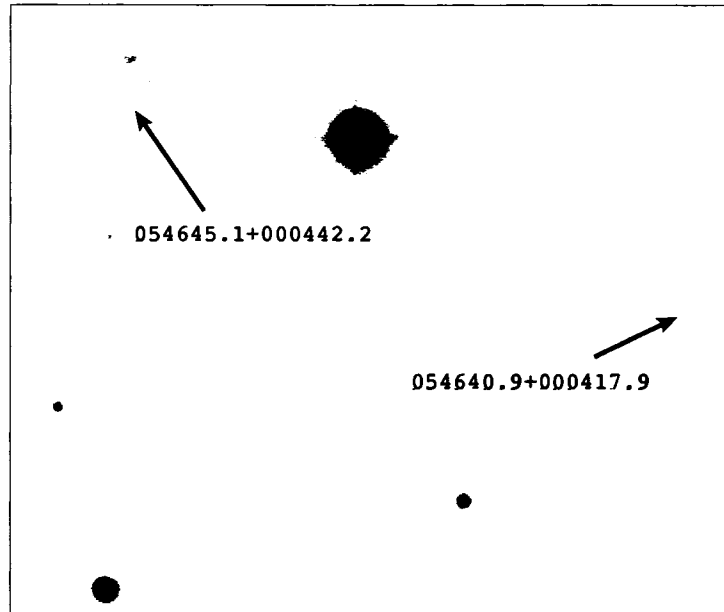
Figure 5.10: H$_2$ objects toward the northern edge of the 2.122 μm map.

knot in the vicinity (054630.6-000426.6) is not detected at all in continuum so most certainly it is shocked hydrogen resulting from a nearby YSO outflow. The star at RA 05:46:30.8, Dec -00:04:22.2 ~ 5" north-east of this knot is barely detected at all in the Digitized Sky Survey (DSS) infrared images, and the star at RA 05:46:29.1, Dec -00:03:48.2 which appears bright in the CFHT-IR maps is weekly detected in the DSS compared to other bright stars in the CFHR-IR maps. This is not at all surprising, as the K-band extinction inferred from the 850 μm flux in Mitchell et al. is as high as a few magnitudes in some regions, implying a visual extinction of $\gtrsim$ 20 magnitudes.

Slightly north of these objects there is bright line emission (and faint continuum emission) associated with core 51 (054630.7-000235.4). This line emission is likely a stellar jet, as will be discussed in further detail in the next chapter.

Very faint line emission is associated with core 47 (054627.8-000052.8), which will be discussed in the next chapter. Since there is no emission in the K continuum image this H_2 is likely emission due to a deeply embedded YSO jet.

Both continuum and line emission are present around core 42 (054633.2+000001.8). The bulk of the double-peaked (two bright sources, spatially close to one another) region appears very bright in the continuum map; a good indication that we are seeing the embedded stellar object(s). The faint, smooth emission directly east of the bright source extending northward is present in both continuum and line images and could be YSO light reflected off of dust. This object has some interesting emission features which appear to be associated with it, including a cluster of H_2 knots. The inferred association of these features with a YSO is explored in the next

chapter.
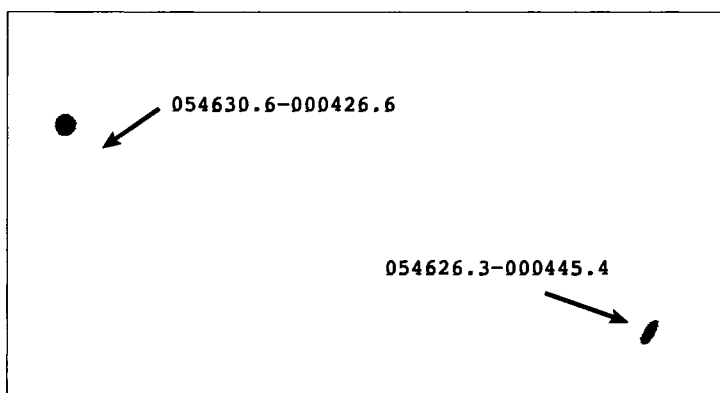
Figure 5.11: H_2 objects in south region of map.

A noteworthy object in both filters is the bright asymmetrical object near the centre of the IR maps (054643.1+000052.2). This object (fig. 5.12) is nearly coincident with sub-mm core 35[1], and will be discussed further in the next chapter. This feature is distinctive because of its bright wisps that extend predominantly in the north and south directions. There are also extensions to the east and west, which are composed mostly of H_2 upon examination of the IR maps; case-in-point the H_2 shock feature at 05:46:43.8+00:00:53, for which a surface brightness has been tabulated (see table 5.3).

About 1 arcminute west of this object lies one of the most interesting features observed in the H_2 map, and it will be discussed in depth in chapter 6. This feature, labeled 054638.8+000050.5 (fig. 5.13), is absent in continuum.[2] The structure of this object appears to fit the profile of a typical bow shock, caused by a stellar jet

---

[1]Known as SSV 19 (Strom, Strom & Vrba, 1976).

[2]There is actually very faint emission in the vicinity of the double-peaked region in the continuum map, but the signal is within the noise level.
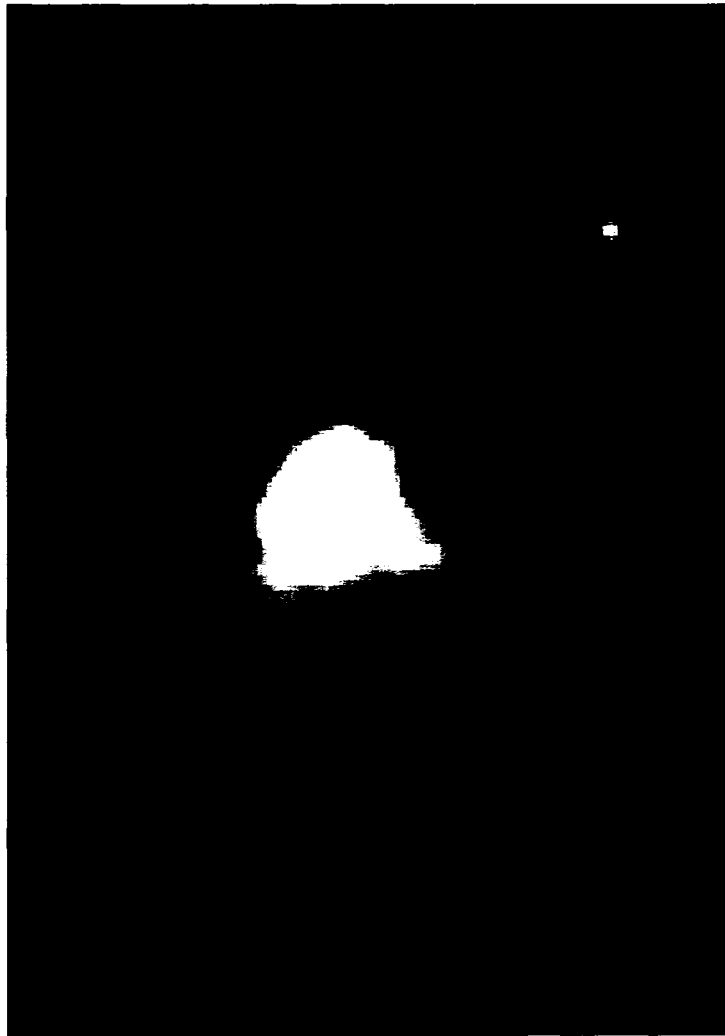
Figure 5.12: H_2 filter image of feature 054643.1+000052.2 (labeled 43.1+052.2 in figure 5.7).

emanating from a YSO outflow.

Further north of the 'bowshock' is a large comma-shaped compact emission feature (054639.3+000114.7) which appears very bright in the H_2 filter. This object will be discussed in chapter 6.
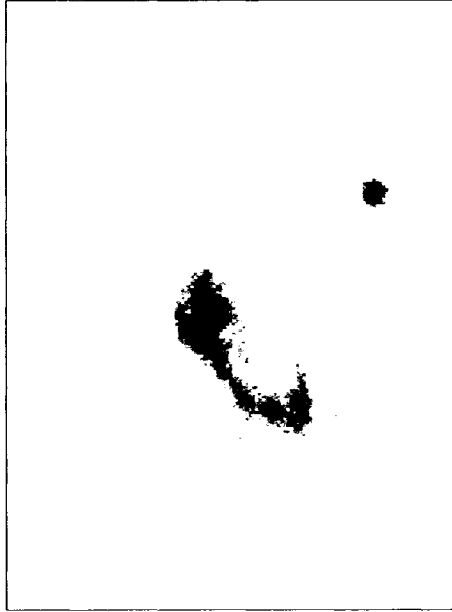
Figure 5.13: "Bow shock" feature 054638.8+000050.5.

A lot of IR structure is visible centred around core 39 (054647.0+000027.0), with bright knots and a few possible stars grouped in a cross-like configuration (see figure 5.14). There is IR emission in the form of a faint arc located at the southern-most point-like feature extending 10 − 15 arcseconds northward. Many of the features however are not point-like, and possess a Herbig-Haro-like appearance. This region is similar in brightness in both filters; an indication that it is likely to be mostly or all continuum. This assumption could not be verified until the continuum flux was subtracted from the line flux, as is shown in tables 5.2 & 5.3. IR photometry of this
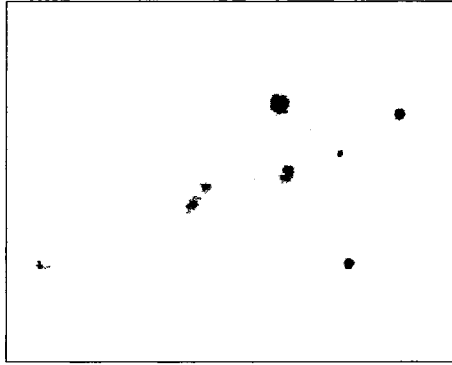
Figure 5.14: From figure 5.8: IR structure 054647.0 + 000027.0 and knot 054649.0 + 000015.0.

object has revealed that much of the nebulous emission is in fact continuum, and only some line emission is present in the central region. However the knot that lies to the south-east of the IR structure is pure H_2 (054649.0+000015.0). The 850 μm mass of this core is calculated to be 2.1 $M_\odot$ (Mitchell et al. 2001). This object will be discussed further in the following chapter.

Table 5.2: IR flux densities of NGC 2068 Objects. Where the flux was measured at a specific coordinate, the RA and Dec are given in the form H:MM:SS.s±D:MM:ss.s in the first column, rather than the associated object name. The 3 objects tabulated in this notation are as follows (table from top to bottom): an H_2 knot near core 42, and two IR knots near core 39.

Object	Continuum	H_2	Pure H_2
	[Jy]	[Jy]	[Jy]
054626.3-000445.4	$(7.0\pm2.0)\times10^{-4}$	$(6.09\pm0.75)\times10^{-3}$	$(5.4\pm1.0)\times10^{-3}$
054627.8-000052.8	not detected	$(3.9\pm2.4)\times10^{-5}$	-
054630.7-000235.4	$(3.2\pm2.0)\times10^{-4}$	$(6.2\pm1.0)\times10^{-3}$	$(5.9\pm1.2)\times10^{-3}$
054633.2+000001.8	$(1.6\pm0.3)\times10^{-2}$	$(9.1\pm1.1)\times10^{-3}$	mixed distribution
5:46:34.6-0:00:11.0	negligible	$(3.7\pm0.9)\times10^{-3}$	-
054638.3+000050.5	negligible	$(1.2\pm0.3)\times10^{-2}$	-
054639.3+000114.7	$(1.9\pm1.4)\times10^{-3}$	$(1.08\pm0.25)\times10^{-2}$	$(8.9\pm3.9)\times10^{-3}$
054641.5+000306.5	not detected	$(9.8\pm7.0)\times10^{-3}$	-
$054643.1+000052.8^3$	$(2.4\pm0.3) \times 10^{-1}$	$(1.94\pm0.08) \times 10^{-1}$	mixed distribution
054645.1+000442.2	unattainable	$(6.5\pm1.0)\times10^{-3}$	unattainable
5:46:47.0+0:00:27.0	$(3.8\pm0.7)\times10^{-3}$	$(2.0\pm0.6)\times10^{-3}$	mixed distribution
5:46:47.7+0:00:24.9	$(3.8\pm0.9)\times10^{-3}$	$(1.9\pm0.5)\times10^{-3}$	mostly continuum
054648.0+000141.6	$(1.1\pm0.3)\times10^{-2}$	$(7.0\pm5.0)\times10^{-3}$	uncert. too large

Table 5.4 contains estimated absolute K magnitudes of six sources in the NGC 2068 protocluster which have associated 2MASS J, H and K band magnitudes. Note that the method used in calculating absolute magnitudes assumes that 1) reddening due to sources external to the YSOs is negligible and 2) that the YSOs are in fact zero age main sequence stars with no (or very little) IR excess, the latter of which is highly improbable. However the absolute K magnitudes are presented as a first order approximation.

Table 5.3: Surface brightness values of IR sources in NGC 2068. Where the flux was measured at a specific coordinate, the RA and Dec are given in the form H:MM:SS.s±D:MM:ss.s in the first column, rather than the associated object name. The 15 objects tabulated in this notation are as follows (table from top to bottom): compact blobs (core 42), 'fan' region (core 42), filament and H_2 knot (core 42); double-peaked structures in bowshock feature; an H_2 knot in "V" configuration; small shock east of core 35; northern patch of H_2 emission; two knots in core 39; region of extensive nebulosity; H_2 knot near core 39; region of extensive nebulosity.

Object/Coordinate	NB cont. Surf. Br. $[Jy/as^2]$	H_2 Surf. Br. $[Jy/as^2]$	Pure H_2 Surf. Br. $[Jy/as^2]$
054626.3-000445.4	$(7.4\pm0.3)\times10^{-5}$	$(7.24\pm0.05)\times10^{-4}$	$(6.5\pm0.1)\times10^{-4}$
054630.6-000426.6	not detected	$(1.28\pm0.07)\times10^{-4}$	-
054630.7-000235.4	$(8.7\pm0.2)\times10^{-5}$	$(1.07\pm0.01)\times10^{-3}$	$(9.83\pm0.01)\times10^{-4}$
5:46:33.2+0:00:01.9	$(9.32\pm0.15)\times10^{-4}$	$(6.7\pm0.1)\times10^{-4}$	mostly continuum
5:46:33.3+0:00:01.0	$(5.16\pm0.15)\times10^{-4}$	$(4.6\pm0.1)\times10^{-4}$	mostly continuum
5:46:34.1+0:00:03.1	$(3.6\pm0.7)\times10^{-5}$	$(3.9\pm0.5)\times10^{-5}$	$(0.3\pm1.2)\times10^{-5}$
5:46:34.7+0:00:30.2	negligible	$(9.1\pm0.5)\times10^{-6}$	-
5:46:35.7+0:00:12.6	negligible	$(6.3\pm0.1)\times10^{-5}$	-
054636.9+000056.7	not detected	$(3.5\pm0.5)\times10^{-5}$	-
054639.3+000114.7	$(1.23\pm0.15)\times10^{-4}$	$(8.9\pm0.2)\times10^{-4}$	$(7.7\pm0.4)\times10^{-4}$
5:46:38.8+0:00:51.2	negligible	$(3.68\pm0.15)\times10^{-4}$	-
5:46:38.9+0:00:49.9	negligible	$(3.64\pm0.15)\times10^{-4}$	-
054639.4+000142.6	$(2.5\pm0.7)\times10^{-5}$	$(4.7\pm0.8)\times10^{-5}$	$(2.2\pm1.5)\times10^{-5}$
054640.5+000052.8	not detected	$(5.1\pm0.3)\times10^{-5}$	-
5:46:42.5+0:03:12.8	not detected	$(6.3\pm0.5)\times10^{-5}$	-
054643.1+000052.2	$(2.1\pm0.3)\times10^{-2}$	$(1.68\pm0.02)\times10^{-2}$	mostly continuum
5:46:43.8+0:00:53.0	negligible	$(1.69\pm0.06)\times10^{-4}$	-
5:46:45.0+0:04:43.5	$(3.0\pm0.6)\times10^{-5}$	$(1.7\pm0.2)\times10^{-4}$	$(1.4\pm0.3)\times10^{-4}$
5:46:47.0+0:00:27.0	$(3.43\pm0.15)\times10^{-4}$	$(3.3\pm0.5)\times10^{-4}$	mostly continuum
5:46:47.7+0:00:24.7	$(2.50\pm0.05)\times10^{-4}$	$(1.25\pm0.05)\times10^{-4}$	mostly continuum
054648.0+000141.6	$(1.15\pm0.05)\times10^{-3}$	$(5.5\pm0.3)\times10^{-3}$	$(4.4\pm0.4)\times10^{-3}$
5:46:48.9+0:02:23.3	$(1.5\pm0.2)\times10^{-5}$	$(1.11\pm0.40)\times10^{-4}$	$(9.6\pm4.2)\times10^{-5}$
5:46:49.0+0:00:15.0	not detected	$(8.0\pm0.3)\times10^{-5}$	-
5:46:49.1+0:02:18.7	$(3.4\pm1.5)\times10^{-5}$	$(7.87\pm1.50)\times10^{-5}$	$(4.5\pm3.0)\times10^{-5}$
054651.4+000026.0	not detected	$(2.0\pm0.4)\times10^{-5}$	-
054654.7-000003.0	not detected	$(5.5\pm0.5)\times10^{-5}$	-

Table 5.4: IR objects in NGC 2068 for which there are published 2MASS J, H and K magnitudes. Extinction toward some of the cores has been inferred from the 2MASS colours. The K band extinctions are calculated following the method of SSV 1976, where $A_V = 14.3E(H - K)$, and $A_K = 0.1A_V$. The absolute K band magnitudes are calculated via $M_K = K - 5\log d + 5 - A_K$, where $d = 415$ pc.

Name	Assoc. Core	K (2MASS)	M_K
054630.7-000235.4	51	15.220	4.74
054633.2+000001.8	42	13.381	3.14
054639.3+000114.7	34	14.099	3.09
054643.1+000052.2	35	8.511	-1.98
054647.0+000027.0	39	13.279	1.42
054648.0+000141.6	32	11.977	1.86

Chapter 6

Discussion of Individual Cores and Implications for Star Formation
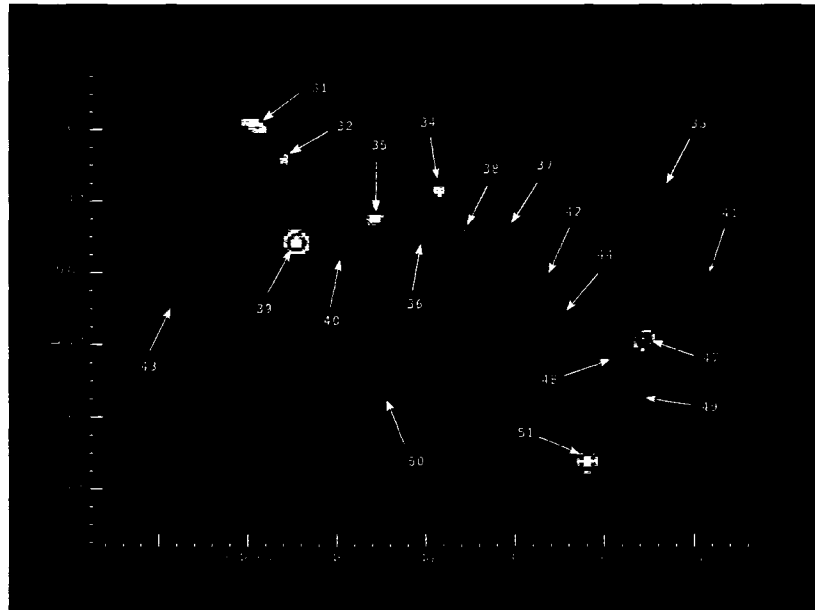
Figure 6.1: 850 micron SCUBA map of NGC 2068. The sub-mm cores are labelled. Figure is adapted from Mitchell et al. 2001.

Sub-millimetre mapping of the NGC 2068 region with the JCMT (Mitchell et al. 2001, Johnstone et al. 2001) has revealed the presence of an embedded protocluster, containing 19 cores of varying brightness arranged in a clumpy, filamentary structure (see figure 6.1). In the previous chapter, NIR images of this region were presented.

It is evident from the varying morphology of the IR emission that the cluster in question is deeply embedded, though there is strong evidence for star formation as made clear by the presence of extended (scattered star light) and more compact (embedded?) narrowband emission, as well as the many shocked molecular hydrogen features. In this chapter the NIR images will be directly compared with the 850 μm map of SCUBA cores, as well as a previously obtained map of high-velocity CO gas (Mitchell et al. 2001). For seven of the sub-mm cores, formaldehyde (H_2CO) spectra was obtained with the JCMT (Tothill and Mitchell 2001). The gas kinetic temperature has been determined by taking an intensity ratio of the 218.2222 (3_{03} - 2_{02}) and 218.4756 GHz (3_{22} - 2_{21}) transitions. As before, North is at the top of all maps, and East is to the left.

H_2CO is a nearly symmetric rotor molecule, and is very sensitive to kinetic gas temperature. Formaldehyde observations are used to determine the temperature of gas in regions where spatial densities are higher than $\sim 10^5$, allowing transitions between energy levels via collisional excitation (see Mangum and Wootten 1993).

The 3_{03} - 2_{02} and 3_{22} - 2_{21} transitions are closely spaced in frequency and can be measured by the same receiver. This greatly reduces calibration uncertainties. An intensity ratio between $K_a = 2$ and $K_a = 0$ transitions of the H_2CO molecule is used to derive T_{kin} based on the method described in Mangum and Wootten (1993), relating kinetic gas temperatures via the Boltzmann equation. The approximation is valid under the assumptions that the region of the molecular cloud is optically thin, the transition excitation temperatures are approximately equal, and the number density is sufficiently high ($n(H_2) \gtrsim 10^{6.5}$ cm^{-3}, c.f. Tothill and Mitchell 2001;

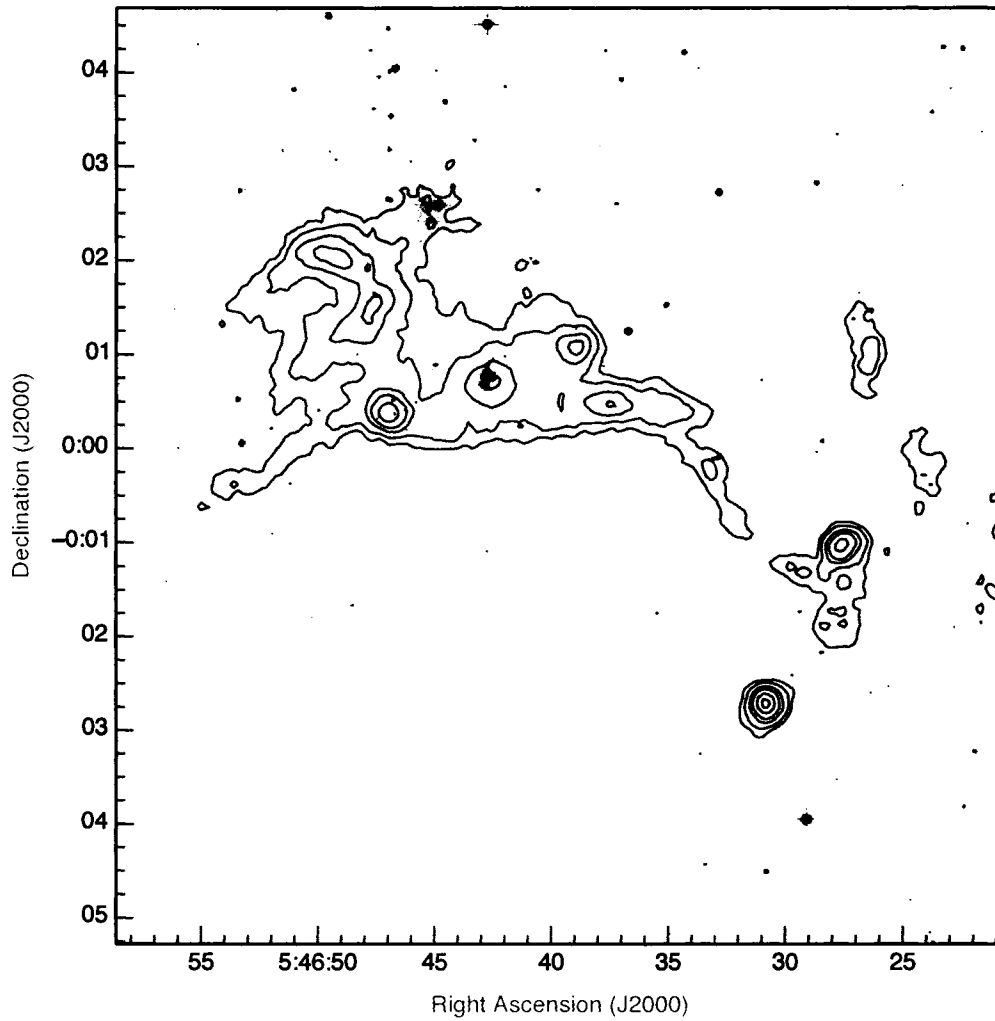Mangum and Wootten 1993, Table 4 and Appendix A).

Figure 6.2: Continuum map with 850 μm contours overlaid. Note how the contours follow the IR emission at $\sim$ RA 5:46:48, Dec 0:02:00.

OriBsmm 31 & 32

Core 31 (fig. 6.1) has a fairly bright 850 μm surface brightness and appears elongated. There is no obvious association with IR objects, however prominent

diffuse nebulosity exists at the north-western boundary in the eastern region of the

850 μm map. It is interesting to note that this bright band of emission discussed in

the previous chapter (arrow in fig. 5.2) is closely correlated with the 850 μm emission

(sub-mm contours, see figure 6.2). This similarity in structure solidifies the idea that

this extensive region of emission is in part made up of scattered starlight from dust,

enabling us to see the physical dust boundary within which the cores exist. As noted

in table 5.3, this region was found to be mixture of continuum and line emission;

the former likely from scattering of starlight from dust, and the latter from UV

fluorescence.

A temperature of 31 K is inferred from the H_2CO spectra (Tothill and Mitchell

2001); somewhat warm for a pre-stellar core. But since no compact IR emission or

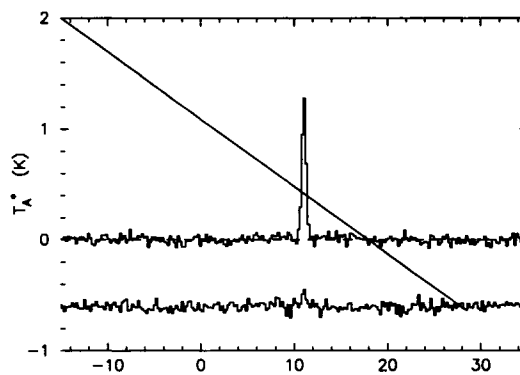Figure 6.3: Core 31. Antenna temperature vs. LSR (local standard of rest) velocity
(km/s)

H-H object is associated with this core, and given the narrow line width of the H_2CO

spectra, it is likely that it is pre-stellar in nature. Line wings would be indicative

of warmer, more energetic gas. Figure 6.4 shows a CO spectral line that has been

taken in the vicinity of cores 31 and 32, at RA 5:46:49.8, Dec +0:02:14.4. ^{12}CO is

optically thick, enabling the gas kinetic temperature to be determined. The CO gas

probes the regions of the core up to a certain point; within the denser regions the

CO becomes too optically thick where as the H_2CO gas is effective in probing the

inner-core regions, where densities are higher. The CO line in this region is bright

with an antenna temperature T_A^* (recall the Introduction, § 1.1) of 50 K . Since the

CO spectra will measure the gas temperature outside of the densest part of the core

(George Mitchell, private communication), it is reasonable to assume that the gas

in this region is warm due to stellar radiation from the young star cluster to the

north-west of the IR maps.

Core 32 however does have an associated IR source lying 6" from the central

core region (054648.0+000141.6, see figure 6.5). This core is similar in appearance
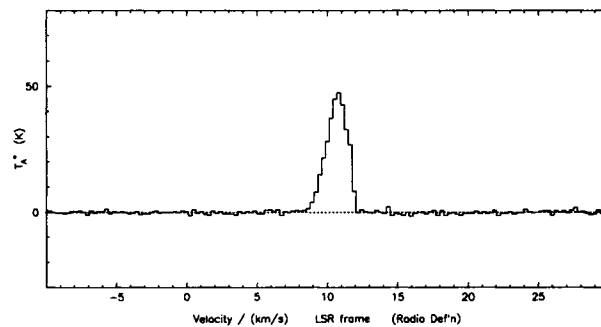
Figure 6.4: ^{12}CO spectral line near location of core 31.

to core 31 in the sub-mm map (fig. 6.1), with an elongated 850 μm shape. It

also has 'trails' of dust emission that extend to the south-east, as is the case for

cores 31 and 39. The H$_2$CO spectrum also shows that this core may be pre-stellar with $T < 26$ K (Tothill and Mitchell 2001), though the bright IR source is likely associated with this core, and hence one can infer that this core is in the very early stages of star formation, and is very deeply embedded. The narrow H$_2$CO spectral line is indicative of cooler more quiescent gas, so the spectra was presumably not sampling the north-west region of the core, where the bright IR feature lies.
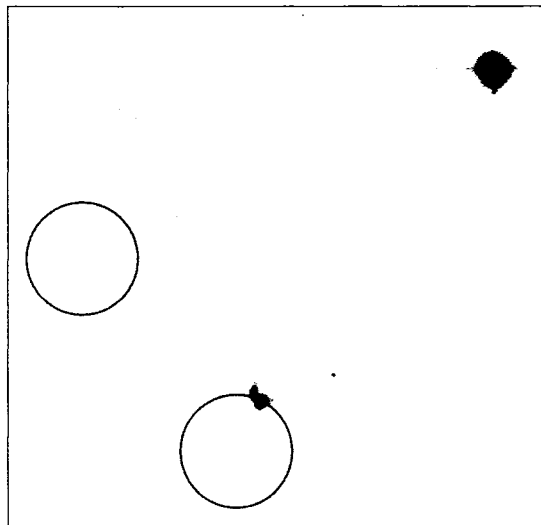
Figure 6.5: IR source 054648.0+000141.6 (H$_2$ filter). 20" circles represent the location of sub-mm cores 31 (left) and 32 (right).

OriBsmm 33

This core has a low 850 μm surface brightness and is less centrally peaked than most of the other cores in NGC 2068. It appears to be part of a filament which also encompasses core 41 to the south-west (both are not very bright in sub-mm emission). No IR emission is seen within 20" of this core, and given the diffuse 850 μm structure, this object is likely pre-stellar in nature.
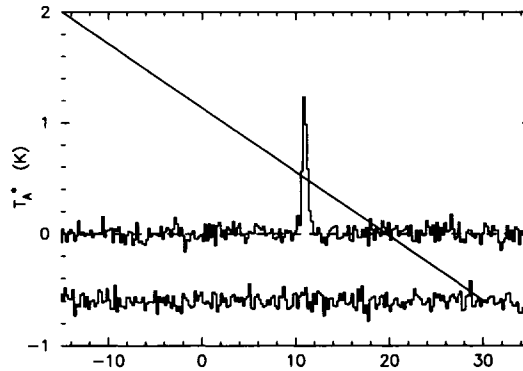
Figure 6.6: Core 32. Antenna temperature vs. LSR velocity (km/s).

OriBsmm 35, 38, 34 & 36

Core 35 has one of the strongest 850 μm fluxes of all of the NGC 2068 cores. In the NB filter, the core region is very bright, and has an asymmetric structure. In the H_2 filter, even more structure is visible; particularly there is a small H_2 filament eastward of the bright IR source 054643.1+000052.2 (see figure 6.7). This filament can be interpreted as shocked molecular hydrogen due to a strong stellar wind. A CO outflow is centred on this core and the H_2 shock feature is located very close to the CO red-wing peak (cf. figure 6.8), solidifying that this filamentary shock feature is shock-excited by a bipolar outflow originating from the YSO contained in core 35.

Westward of 054643.1+000052.2 is the blue wing of CO gas, however there are clearly at least two regions where the higher velocity gas shows peak velocities. It is possible to explain two of the peak regions as both emanating from OriBsmm 35; the northern and southern (or westward) wisps. Perhaps the molecular material is more dense to the east, and the emission is more visible westward of the core (near the blueshifted CO) because that is where it is being blown into a cavity. Or it's

possible that the westward emission is simply more visible because that region is less embedded, as the blue-wing of CO would indicate. The blueshifted peak lies 22" south-west of the core's centre. Core 35 is almost certainly responsible for the observed bipolar CO outflow.
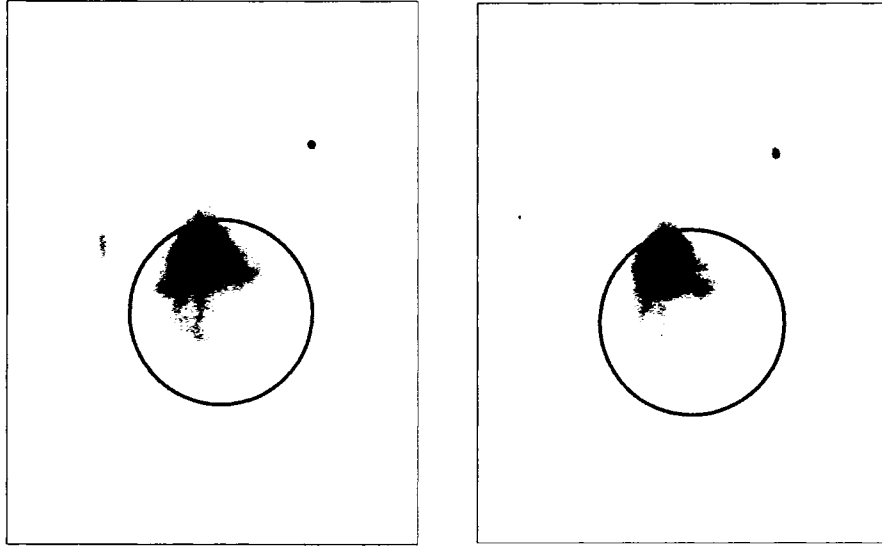
Figure 6.7: Core 35 in H_2 filter (left) and the continuum filter (right). The 20" circles are at the location of the sub-mm core.

The H_2CO spectra of this core (figure 6.9) is broader than those of cores 31 and 32, lending support to the observed stellar activity (outflow, bright K continuum and H_2 emission). The inferred kinetic temperature is $\sim$ 44 K (Tothill and Mitchell 2001), notably warm for a sub-mm core.

Core 38 has a strong surface brightness in the 850 μm map.(figs. 6.1, 6.2). There is a compact, unresolved source within 10" of the core centre, and it is difficult to say whether or not this source is the embedded YSO, or rather a foreground object.
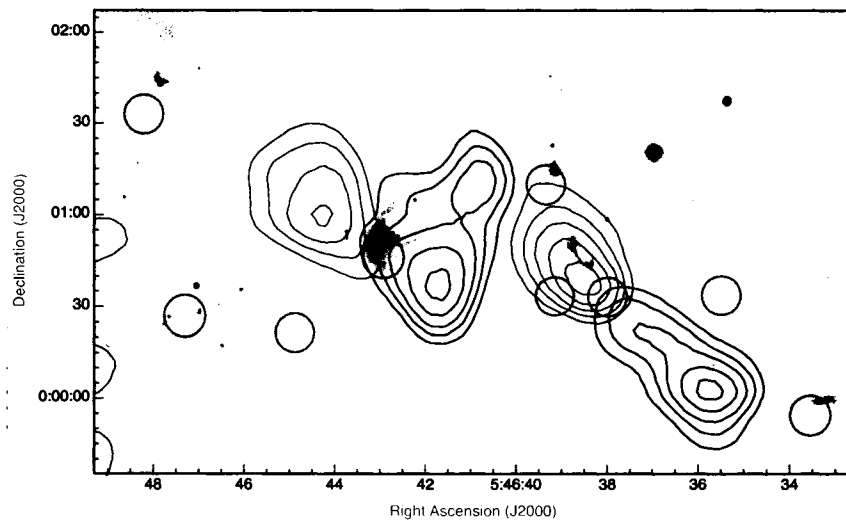
Figure 6.8: Field 1 region in H_2 filter. Red- and blueshifted ^{12}CO wings are shown. Grey circles represent the 14" SCUBA beam size, and are located at the positions of sub-mm cores. Core 42 is located at the bottom right (south-west), and core 38 is located at the origin of the west-most CO outflow. Core 34 is located near 054639.3 + 000114.7.
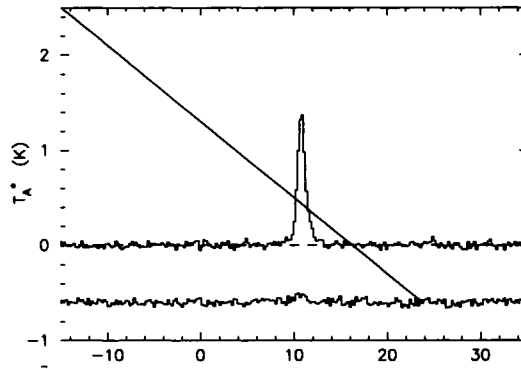
Figure 6.9: Core 35. Antenna temperature vs. LSR velocity (km/s)

The elongated blue wing of CO (fig. 6.8) helps to solidify the idea that the bipolar outflow is emanating from this core, and thus it most definitely contains a forming star.

There are several cores in the vicinity of the H_2 bowshock-like feature 054638.8+000050.5. One interpretation is that the curved shape of this object is caused by winds from YSOs impacting upon an H_2 clump causing shock-excitation at the tip but allowing for material to be blown away on the sides. The bright double-peaked structure (see fig. 6.12) could be a second dense wind-blown shock-excited region which is working its way continually away from core 38 located to the south-west (figure 6.8). The projection of this feature is not obvious given these circumstances, though in looking at the figure it is tempting to associate this feature with the red wing of CO, thereby insinuating that it is associated with core 38. Another perhaps more credible interpretation is that this object is a bow shock as a result of a stellar jet. Where outflow speeds are highly supersonic, high-velocity (> 100 km/s) gas may undergo shock compression as it is heated. If 054638.8+000050.5 is indeed a

bow shock, then it can't be associated with core 38 and its bipolar outflow. However without H_2 spectra, it is not possible to infer the projection of this bow shock-like feature on the sky.
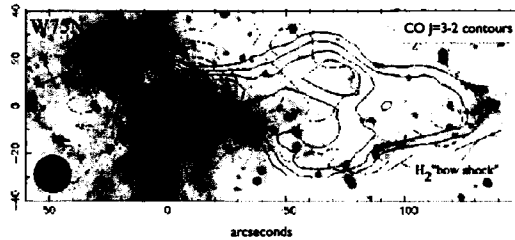
Figure 6.10: H_2+continuum image of molecular outflow of W75N (JCMT). The blueshifted and redshifted CO gas is shown as dashed and solid lines, respectively. Figure is adapted from Davis, Smith & Moriarty-Schieven 1998, the JCMT newsletter, number 10.

In interpreting this object as a bow shock, the southern-most edge can be likened to a working surface, which would indicate that the parent outflow is located toward the *north-east* (figure 6.10 shows a great example of entrained gas within a molecular outflow, i.e. an H_2 bow shock and high velocity CO gas). When examining figure 6.8, core 34 (near-IR source 054639.3+000114.7, the 'comma shape') is located north-east of 054638.8+000050.5, though there is no corresponding CO bipolar outflow to support a scenario ascribing core 34 to be responsible for the bow shock feature. There is however some patchy H_2 emission located $\sim$ 25" north of this core (054639.4+000142.6, see figure 6.12). Perhaps the bowshock is being driven by one jet from core 34 and the patch is shocked H_2 resulting from a YSO jet emanating from the other side of the core.

The compact IR source 054639.3+000114.7 is seen just 5" from the centre of core 34. The IR object is detected in the narrowband continuum but is much brighter in the line filter. It is possible that core 34 is very deeply embedded, as the surrounding nebulosity would indicate, and cloud material is being shocked by young stellar winds in the immediate vicinity of the core as well as farther away from the core as a result of outflows/jet activity.

The H_2CO spectra of this core shows faint wing emission, which supports the idea that the core contains a forming star. The local thermodynamic equilibrium temperature of this core may be as high as 68 K (Tothill and Mitchell 2001).
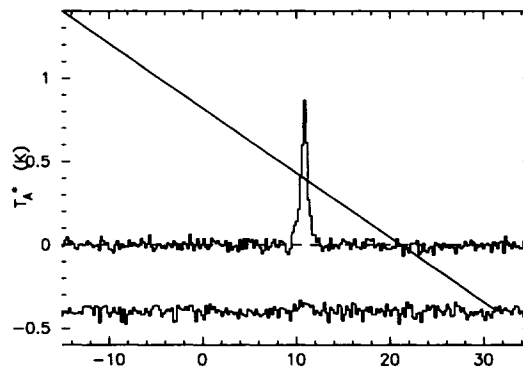
Figure 6.11: Core 34. Antenna temperature vs. LSR velocity (km/s)

The 850 μm flux of core 36 is fainter than that of other nearby cores. There is a small H_2 patch located $\sim$ 20" north-east of this core (054640.5+000052.8), however this patch is also close to cores 35 and 34. Core 36 is likely pre-stellar.
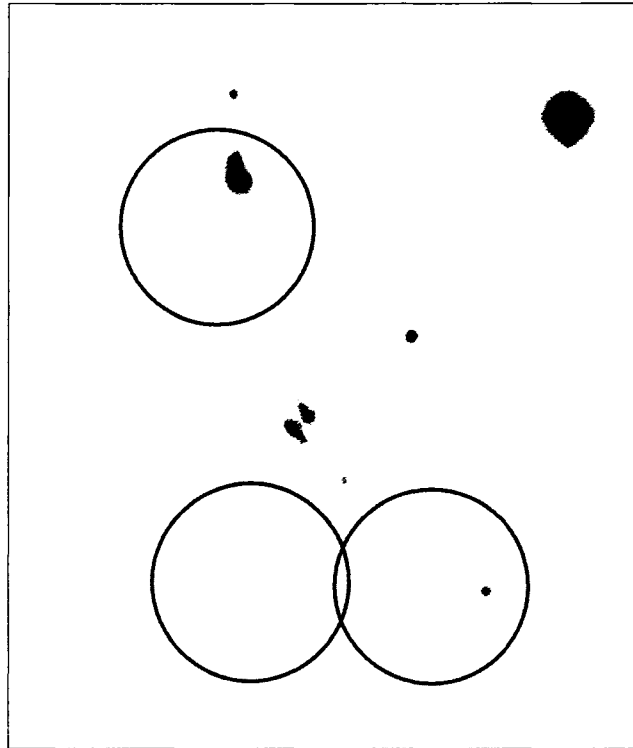
Figure 6.12: H_2 "bowshock" feature and compact H_2 blob at the location of core 34. The lower right and lower left circles are at the locations of cores 38 and 36 respectively.

OriBsmm 37, 42

In the H_2 images, a thin filament[1] is located < 15 arcseconds west of core 37, and a compact H_2 patch is located within 20" (see figure 6.13). However, this core lies outside of the CO map, so it is not possible to link the filament directly to a SCUBA core. Given the appearance of cores 37 and 42 in the SCUBA and CFHT-IR maps, it is more likely that this filament is associated with a protostar embedded in core 42.

---

[1]See table 5.3 for surface brightness of the filament.

Core 42 lies within 10" of the bright binary-like IR source, which has an abundance

of pure H_2 emission in the vicinity. The bright IR source itself is mostly continuum

emission. Molecular hydrogen knots to the south-east and the H_2 filament north-east

of this object are indicative of shock excitation by a YSO wind. Given the semi-

circular orientation of the H_2 features, the embedded protostar may be blowing out

a bubble-wind which is shocking denser regions of the medium.
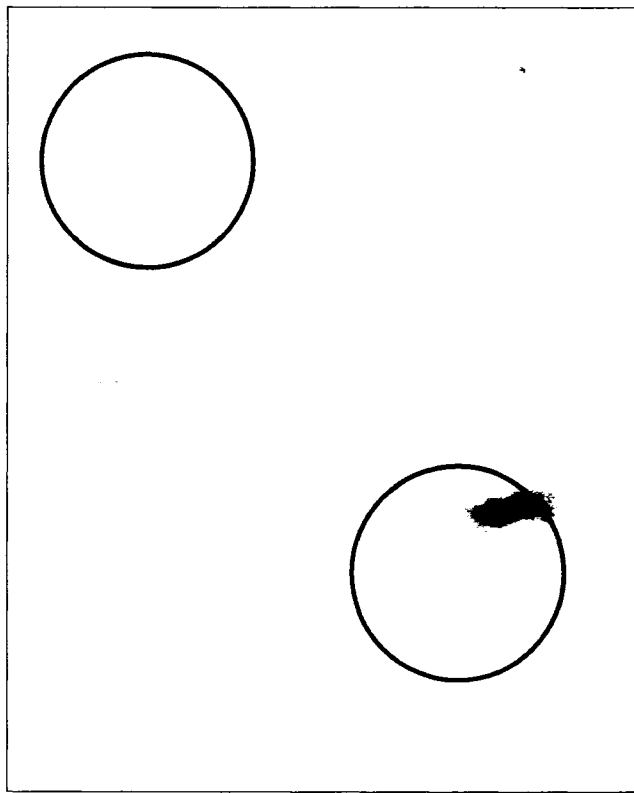
Figure 6.13: IR sources associated with core 42 (right) and 37 (left) in the H_2 filter. The knots and the filament are H_2 features and are absent in the narrowband image.

OriBsmm 39, 43

There is both H_2 emission and continuum emission associated with core 39. There are at least 2 unresolved sources nearby which may be stars rather than embedded YSOs. Further to the west of the core, there is a pure H_2 knot (054649.0+000015.0), likely shocked hydrogen from an outflow coming from the core, which is quite bright in the sub-mm map. This core likely does contain a forming star (or stars), and the IR images are showing scattered star light from a YSO embedded in the core, as well as shocked molecular hydrogen (see figure 6.14).
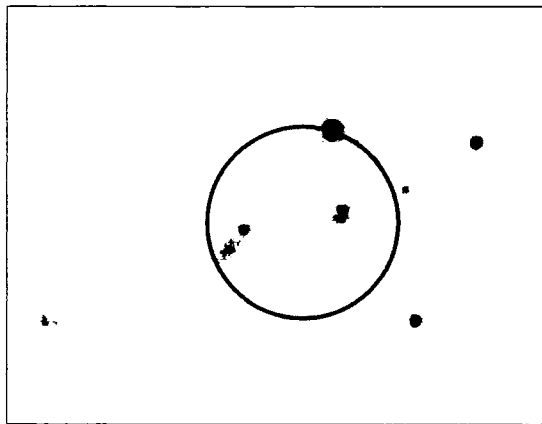
Figure 6.14: IR sources (H_2 filter) associated with core 39 (grey circle).

The H_2CO inferred kinetic temperature of this core is 31 K, which is warm for an embedded core. The H_2CO spectrum of this core (fig. 6.15) shows broadened wings, in support of the idea that this core contains one or more forming stars.

The very faint H_2 knots in field 2 (cf. figure 5.8) are located in the vicinity of cores 39 and 43, but it is not obvious that they are shocked hydrogen as a result of a stellar outflow from one of these cores. The likelihood that these knots are associated

with core 43 is small since this core shows no signs of active star formation. There

is some interesting structure in the 850 μm image however, as core 43 seems to be

connected with core 39 via a dusty filament.
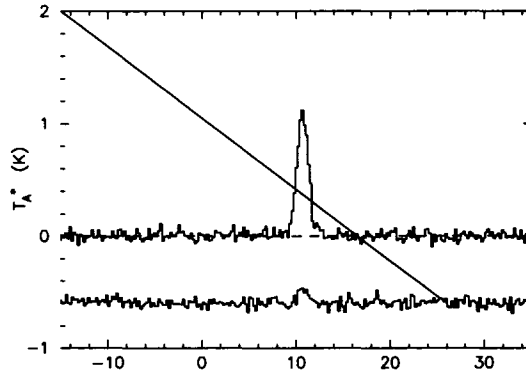
Figure 6.15: Core 39. Antenna temperature vs. LSR velocity (km/s)

OriBsmm 40, 41

If there were evidence of an outflow present, perhaps one could make the associ-

ation of core 40 with the wind-blown appearance of OriB 35, but given the spatial

distance of > 30 arcseconds and the faint dust emission of core 40, this scenario is

unlikely. Core 41 is very faint in the sub-mm map and lies at the boundary of the

CO map. There is no visible IR source associated with either of these cores, and

they are likely pre-stellar in nature.

OriBsmm 44

There is no IR emission in the images which would indicate an association with

this faint core. Note again, the dusty filamentary structure which connects several

of the cores.

OriBsmm 47

This core has no associated NB emission, and appears uninteresting in the K continuum map. However there is very faint H_2 emission at the centre of the 850 micron peak (see figure 6.16). This core is centrally peaked and has very high sub-mm surface brightness. The fact that shocked hydrogen is visible in the vicinity of the core (in fact, it is coincident), is strongly suggestive that this core contains a forming star. The faint H_2 emission can be interpreted as a partially embedded YSO jet.

Figure 6.16: Core 47: faint H_2 emission is visible at the 850 μm peak (grey contours).

The H_2CO spectra of this core is very broad, implying energetic gas motions toward the centre and hence the onset of star formation (see fig. 6.17).
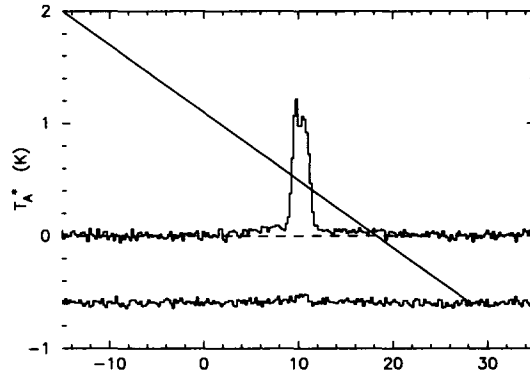
Figure 6.17: Core 47. Antenna temperature vs. LSR velocity (km/s)

OriBsmm 48

This core has a low 850 μm surface brightness and is quite close to core 47, but it is unlikely that the faint H_2 object 054627.8-000052.8 is associated with this core. There is no other IR emission in the vicinity that would indicate an IR association, hence this core is likely pre-stellar.

OriBsmm 49

There is no IR emission which appears to be associated with this core.

OriBsmm 50

This core is just barely in the IR fields. There is no visible IR source associated with this core in the images.

OriBsmm 51

Bright H_2 line emission is visible and almost coincident with the sub-mm core, and there is clearly a bipolar outflow (see figure 6.18). This bright H_2 can be interpreted as a jet. IR emission is also visible in continuum, though it is much fainter (table 5.3). No H_2 emission is visible in association with the high velocity CO gas in the region, and so perhaps this region of the field is dense with gas and dust, and shocked molecular hydrogen is deeply embedded, rendering it undetected. The H_2CO spectra (figure 6.19) shows very broad and asymmetrical wings, and is indicative of warm, high-velocity gas.

Further, the CO bipolar outflow associated with this core lends support to the idea that this core contains an embedded forming star. The orientation of the outflow is not known, but it is possible that we are seeing the blueshifted YSO jet, and the other jet on the far-side is directed away from us plunging deeper into the cloud, hence we do not see it. The fact that continuum emission is detected at the same location as the line emission could be indicative that we are seeing the jet nearly pole-on, and as material is being blown away the embedded YSO is emerging, making itself visible.
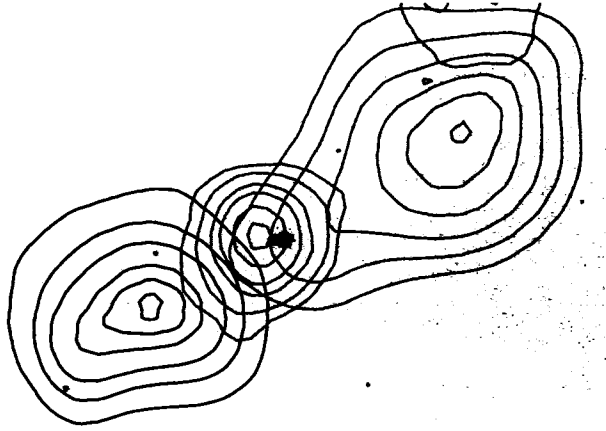
Figure 6.18: 2.122 μm image of core 51 (bright jet) with 850 μm contours (grey) and CO red and blueshifted high-velocity wings. Data has been adapted from Mitchell et al. 2001.
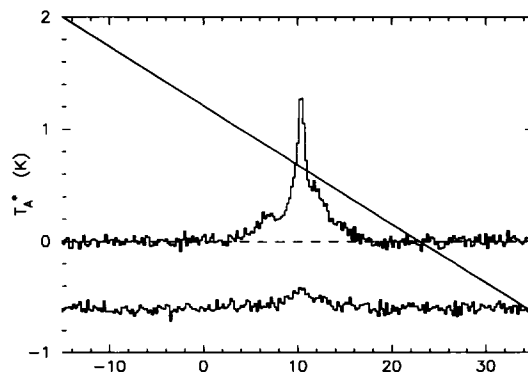
Figure 6.19: Core 51. Antenna temperature vs. LSR velocity (km/s).

Chapter 7

Summary

Recent sub-millimetre mapping of the NGC 2068 region in the Orion B Molecular Cloud has revealed the presence of a group of cores which appear to be an embedded protocluster in the early stages of star formation. In this thesis I have presented two near-infrared maps of the region; one using a narrow band filter centred on the 2.122 μm line of H_2 and the other using a narrowband filter in the adjacent continuum. In the interpretation of these infrared observations I have made use of published CO maps as well as some unpublished H_2CO spectra.

Of the 19 cores in the 850 μm map, 7 of them show signs of associated IR emission. Several of the more diffuse sub-mm cores appear asymmetric in the 850 μm image (figure 6.1), and most of them show no associated IR emission and no sign of star formation. The three cores which are centrally peaked and brightest in dust continuum emission (39, 47 and 51) all have associated IR emission in various forms; line and continuum extended emission and knots, line emission only, and bright, compact line and continuum emission, respectively.

Cores 31 and 32 are both bright in 850 μm emission, and though they lack apparent spherical symmetry, core 32 shows an associated IR source and hence likely contains a forming star. Core 32 is a Class 0 or Class I candidate. Core 31 may be pre-stellar in nature, or perhaps it is a protostar but the K-band emission

is undetectable due to high extinction. Cores 34 and 35 show strong signs of star formation with bright narrowband and H_2 emission, as well as a CO outflow (core 35), and are likely Class 0/I and Class I objects respectively. The evidence of a bipolar outflow for core 38 suggests that this core also contains a deeply embedded forming star. Conversely, core 36 has no outflow or IR counterpart, and appears to be pre-stellar. The centre-to-centre spatial separation between cores 36 and 38 is only $\sim$1000 AU, and given the diffuse and extensive nature of sub-mm core envelopes, it's possible that core 38 is accreting much of the would-be available mass from the vicinity of core 36, inhibiting the chance for core-collapse in the latter. There could be a similar case made for cores 48 and 47, the latter of which is centrally peaked, having the highest 850 μm flux of any sub-mm core in the NGC 2068 protocluster (2.44 Jy; Mitchell et al. 2001). The fact that core 47 shows faint H_2 line emission but no continuum emission indicates that it is a Class 0 YSO, with powerful highly-collimated outflows, conceivably oriented nearly perpendicular to the plane of the sky. It's probable that the YSO outflow and jet(s) are shock-exciting the molecular hydrogen but are still very young, and have not had the chance to blow away much of the surrounding interstellar material. Core 51 (850 μm flux of 2.40 Jy, Mitchell et al. 2001) shows both continuum and line emission at the same location, as well as a bipolar CO outflow. We are seeing evidence for both a shock-excited jet, and the embedded (reddened) YSO itself. Core 51 is presumably a Class 0 or early Class I object. It is likely that if this YSO were a later Class I object, we may see traces of outflow activity in the optical. Core 39, also bright in 850 μm emission (2.42 Jy; Mitchell et al. 2001) has associated narrowband and line emission in the

form of diffuse structure and compact knots, both resolved and unresolved. This core most definitely contains one or more forming stars. Lack of CO data makes it difficult to determine if there is a bipolar outflow, though one would expect one to be present. Core 42 shows clear signs of star formation with the presence of several nearby shocked H_2 structures and a very bright doubly-peaked continuum source (possibly a binary?) in the IR maps. Nearby diffuse continuum emission is indicative of scattered YSO light off of dust grains. Cores 33, 37, 40, 41, 43, 44, 48, 49 and 50, and possibly 31 and 36 are likely pre-stellar.

In all, the following 8 cores in NGC 2068 are presumably forming stars: 32, 34, 35, 38, 39, 42, 47 and 51. These cores are either Class 0 or Class I objects, though it is difficult to deduce which stage corresponds to which YSO since there is a lack of mid-infrared spectral information. Given the deeply embedded nature of these cores, classification of these YSOs is biased toward Class 0 objects since high extinction and uncertainty in inclination angle may inhibit the detection of YSO jets, which become observable only through the clearing of interstellar media as a result of the outflow activity.

The protocluster south of NGC 2068 is $\sim$ 6 x 8 arcminutes in extent, corresponding to a spatial size of approximately 1 pc, and nearly half of the Sub-millimetre cores over the entire extent of this region show signspots of star formation. This protocluster lies roughly in between two other well-known star forming regions in Orion B North. About six degrees north of the NGC 2068 protocluster is a well-known outflow region, NGC 2071, and $\sim$10 arcminutes south of NGC 2068 is the

well-known star forming region Herbig-Haro 24-25-26. Sub-millimetre mapping of Orion B (Mitchell et al. 2001) shows the presence of compact cores in these two regions. OriBsmm 11 (NGC 2071) is the brightest sub-mm core mapped in Orion B North with a total 850 μm flux of 30.29 Jy (Mitchell et al. 2001) and is a well-known outflow region; it is also a site of very prominent shocked H_2 emission. Near IR imaging of NGC 24-26 (Davis et al. 1997) reveals narrow band K continuum point sources, as well as prominent extended and knot-like H_2 features (H-H objects). HH 24-26 also contains at least three optical outflows; another definite sign of active star formation. Given the spatial separation of these three star forming regions, it is unlikely that one particular cluster is 'aware' of the fact that any other cluster in the cloud contains clumps which are undergoing core collapse. Yet all three regions contain Class 0 and Class I YSOs and outflows, implying that they are all of comparable age.

Low star formation efficiency (isolated star formation) is associated with turbulently supported regions of molecular clouds. It is this turbulent pressure that is responsible for the overall stabilization of the molecular cloud. The low-mass cores in these regions are thought to collapse by the process of ambipolar diffusion (Lada and Lada 2003). However, efficient star formation resulting in the collapse of several pre-stellar clumps out of a filament or chain of cores is known to occur in regions which lack turbulent support due to the dissipation of turbulent energy in density-enhanced regions, as was briefly discussed in § 1.4.2. Once turbulent support is lost, fragmentation and core-collapse may ensue given the appropriate physical

conditions.

It is reasonable to believe that the protocluser in NGC 2068 has lost turbulent support, resulting in the collapse of several pre-stellar cores. Near-IR and sub-mm observations of the Orion B Molecular Cloud have revealed the nature of the embedded protoclusters. The sub-mm protoclusters, though widely separated, all appear to show signs of early and active star formation. These observations lend support to the idea of coeval star formation, in which various regions throughout a molecular cloud lose turbulent support on similar timescales, as is predicted by simulations of compressible turbulence in molecular clouds (c.f. Klessen and Burkert 2000).

Appendix A

A.1 Pre-Main Sequence Ages

While a lot of useful information about young embedded objects in molecular clouds is made available by observations at a few different wavelengths, YSO ages are poorly constrained unless sufficient observations across a wide range of wavebands are made, in order to obtain a spectral energy distribution of the source.

The mass-luminosity relationship for PMS stars is a function of time, and the K-band luminosity varies as

$$L_K \propto M^{1.6}\, t^{-2/3} \tag{A.1}$$

(Zinnecker et al. 1993) which makes age determination of shrouded YSOs difficult.

In deriving ages for YSOs, several assumptions must be made. One method is to assume a universal IMF for all protoclusters. With an adopted initial mass function, model K-band luminosity functions can be derived. The luminosity functions can then be used to predict the observed counts expected from such a star cluster.

More often, when enough data is available, young stars can be transformed (plotted) to a theoretical evolutionary track (usually L vs. $T_{\rm eff}$), mapped from the observational colour-magnitude plane (c.f. Herbig and Dahn 2002, Lada and Lada 2000, Kenyon and Hartman 1995). Unfortunately, the calculation of YSO ages is beyond the scope of this thesis, given the limited set of observational data. With

additional data spanning from the L-band (3.5 μm) longward to the near-sub-mm

regime, more direct constraints on YSO ages could be made with the construction

of SEDs.

Appendix B

B.1   Data Reduction - Nomenclature

I will refer to one **frame** as being <u>one</u> complete set of **pointings** in one **field**. One

field is defined as a set of pointings that are spatially close together (5 arcseconds)

for future alignment (and co-addition) which results in increased signal to noise.[1]

For instance, if locations A and B are in field 1, and if one took three exposures (or

integrations) at pointing A, then dithered (or jiggled) to pointing B and took three

exposures, then back to A with 3 exposures, then finally to B with three exposures,

there would be a total of two frames taken for field 1. When possible, observations

were carried out such that the order was: sky - frame1,field1 - sky - frame2,field1 -

sky - frame1,field2 etc. As with CFHT-IR raw images, each exposure at pointing A

(and similarly for B) is stacked; i.e. the images are in a data cube and have to be

unstacked before they are usable.

B.2   Method

2003 data: For the sky images, there were not always three integrations per

pointing. In order to save time, the sky frames would be obtained as follows: sky

(2 frames) - source 1 - sky (1 frame) - source 1 - sky (2 frames) - source 2 - sky (1

---

[1]Fields are spaced 3 arcminutes apart centre-to-centre.

frame) etc. With this procedure the sky with 2 frames could be used twice; once for each adjacent source field (given that the same filter was used in each case). For each of the sky images with two frames, each image was sliced with *imslice* and all of the pointings (including the single frame sky for the corresponding field) were recombined using the task *imcombine* with *combine* set to *median*, so as to eliminate the presence of stars (using *average* instead of *median* would not be successful in keeping only the midpoint value in brightness corresponding to each pixel location).[2]

The process was slightly more complicated for the source images. The source images were sliced the same way (with *imslice*), however were re-combined differently. Unlike the sky frames, for which stars or other astronomical objects are undesirable, the sliced source images were recombined by pointing only (separately for different frames) using the task *imsum* with *option* set to *average*. In practice now one would be left with 10 images; 2 sets of 5 pointings. The filenames of the source images and pre-combined sky images were of the following syntax:

f(#)_(filter)_(sky or source)(number in sequence)(a,b,c,d or e)[3]

where

- the '#' is the field number, 1-6 or 9

---

[2]In fact, no stellar sources were visibly detectable on the median sky images. However when the median sky image was subtracted from the corresponding source images, visual inspection revealed the presence of residual stellar flux which had been left over from the medianing process. This did not affect the photometry, as when the sky signal was subtracted from the source signal during aperture photometry, a large enough patch of sky was used.

[3]In hindsight, it would have saved me a lot of time had I somehow labeled my files according to the dates which they were created. Keeping a log book is helpful but one still has to spend many minutes thumbing through pages to try and recall what one had done in the past in order to create a certain file.

- 'filter' was either 'h2' or 'kc'

- 'sky or source' was designated by either 'sk' or 'so'

- 'number in sequence' was the frame number of that one field in question (either 1, 2 or 3)

- 'a, b, c, d or e' correspond (usually)[4] to the dither position, with 'a' being the central position of the 5-point dither pattern.

For the median sky frames, the syntax was similar: f(#)_(filter)_sk(set of source frames 1 or 2). Slicing and sky-subtraction were carried out using *cl* scripts.

For each of the 10 source images, the corresponding median sky frame was subtracted from it with *imarith*, and the 'so' was replaced by 'ss' in the filename.

The flat field images were sliced with *imslice* and recombined correspondingly using *imcombine*, with *combine* set to *average*. The averaged 'lamp off' flat field image was subtracted from the averaged 'lamp on' flat field image with *imarith*. The subtraction is needed in order to remove the signal that is received from the IR-emitting dome wall (background). This resulting image was divided by its mean value, also with *imarith*. This final flat field image is referred to as a normalized flat field. For this normalized flat (one in each filter), a pixel mask was constructed. A range of values close to 1 were defined (values between 0.5 and 2.0), and any pixel having a value below or above this range (hot or dead pixels) was tagged, and hence

---

[4]Sometimes the telescope's pointing was slightly off.

would be ignored during the flat fielding process. This bad-pixel mask was made using the task *threash* within the KAPPA package. At this point, the remaining FITS files were transformed into NDF files using the task *convert*. Then each sky-subtracted image was flat-fielded using the 'bad pixel mask' flat. The resulting sky-subtracted flat-fielded images then displayed these bad pixels, but were eliminated once the images were mosaicked together. Each image was flat-fielded using the task *div* in KAPPA, which divides each sky-subtracted image by the flat field image of the correct filter. an 'f' was appended to the end of each filename.

For each filter, the 10 images in one field were then aligned using the automated tasks *findobj, findoff* and *register* in CCDPACK. *findobj* scans the given set of images for point sources common to all of the images, and *findoff* then finds the offsets of these sources in each. *register* then registers the images such that they are pixel-aligned. When there were not enough point sources in each field, this process would not work, so the semi-automated process *pairndf* was used instead along with *register*. After either process, *tranndf* was run on each image. This script adds the extension -trn to each filename, which is needed in order to make a mosaic of (i.e. attach) the images. This process was carried out by *makemos* (CCDPACK).

References

- André, P., Ward-Thompson, D., Barsony, M., 1993, ApJ, 406, 122

- André, P., Ward-Thompson, D., Barsony, M., Protostars and Planets IV, 1997

- Bachiller, R., 1996, ARA&A, 34, 111

- Bally, J., Yu, K. C., Rayner, J., Zinnecker, H., 1998, AJ, 116, 1868

- Binney, J., and Tremaine, S., Galactic Dynamics, Princeton University Press, 1994

- Davis, C. J., Ray, T. P., Eisloffel, J., Corcoran, D., 1997, A&A, 324, 263

- Davis, C. J., Smith, M. D., Moriarty-Schieven, H., 1998, MNRAS, 299, 825

- Dyson, J. E., and Williams, D. A., The Physics of the Interstellar Medium, Institute of Physics Publishing, 1999

- Elmegreen, B. G., 1998, ASP Conference Series, Vol. 148, eds. C. E. Woodward, J. M. Shull and H. A. Thronson, Jr., p.150.

- Goodwin, S. P., Whitworth, A. P., Ward-Thompson, D., 2004, A&A 414, 633

- Grosso, N., Montmerle, T., Feigelson, E. D., Forbes, T. G., 2004, A&A, 419, 653

- Heiles, C., Goodman, A. A., McKee, C. F., and Zweibel, E. G., Protostars and Planets III, 1993

- Johnstone, D., Fich, M., Mitchell, G. F., Moriarty-Schieven, G., 2001, ApJ 559, 307

- Klessen, R., 2004, Habilitation Thesis, Potsdam University, astro-ph/0402673

- Klessen, R. S., Burkert, A., 2000, ApJS, 128, 287

- Kwok, S., 2002, Physics and Chemistry of the Interstellar Medium, University Science Books, 2005

- Lada, E. A., Bally, J., and Stark, A. A., 1991, ApJ, 368, 444

- Lada, E. A., DePoy, D. L., Evans, N. J. II, and Gatley, I., 1991, ApJ 371, 171

- Lada, E. A., 1992, ApJ, 393, L25

- Lada, C., 1987, IAUS, 115, 1

- Lada, C. J. and Lada, E. A., 2003, ARA&A, 41, 57

- Larson, R. B., The Physics of Star Formation, Rept.Prog.Phys. 66 (2003) 1651

- Li, W., Evans, N. J. II, and Lada, E. A., 1997, ApJ, 488, 277

- Mac Low, M-M., Simulations of Magnetohydrodynamic Turbulence in Astrophysics, eds. T. Passot & E. Falgarone, Lect.Notes.Phys. 614 (2003) 182

- Mac Low, M.-M., and Klessen, R., Rev.Mod.Phys. 76 (2004) 125

- Mangum, J. G., and Wootten, A., 1993, ApJ 89, 123

- Mitchell, G. F., Johnstone, D., Moriarty-Scheiven, G., Fich, M., and Tothill, N. F. H., 2001, ApJ, 556, 215

- Mitchell, G. F., 1991, Graduate Workshop on Star Formation, Université de Montréal. eds. J.-P. Arcoragi, P. Bastien, R. Pudritz. p. 81.

- Sasao, T., 1973, PASJ, 25, 1

- Shu, F., 1977, ApJ, 214, 488

- Skinner, C. J., 1996, Instrument Science Report NICMOS-014

- Stahler, S. W., Palla, F., Ho, P. T. P., Protostars and Planets IV, 1997

- Strom, K. M., Strom, S. E., Vrba, F. J., 1976, AJ, 81, 5

- Tothill, N. F. H., and Mitchell, G. F., 2001, The Promise of the Herschel Space Observatory. eds. G. L. Pilbratt, J. Cernicharo, A. M. Heras, T. Prusti, and R. Harris, ESA-SP 460, 503

- Thronson, H., A., Jr, Harper, D. A., Bally, J., Dragovan, M., Mozurkewich, D., Greenhouse, M. A., Schwartz, P. R., Smith, H. A., Bieging, J. H., Loewenstein, R. F., Lada, C. J., 1986, AJ, 91, 1350

- Weintraub, D. A., Goodman, A. A., and Akeson, R. L., Protostars and Planets IV, 1997

- Williams, J. P., de Geus, E. J., and Blitz, L., 1994, ApJ, 428, 693

- Vázquez-Semadeni, E., Ostriker, E. C., Passot, T., Gammie, C. F., and Stone, J. M., Protostars and Planets IV 1997

- Zinnecker, H., McCaughrean, M. J., Wilking, B. A., Protostars and Planets III 1993